LETTER

doi:10.1038/nature13664

Sensory-evoked LTP driven by dendritic plateau potentials *in vivo*

Frédéric Gambino[1]*†, Stéphane Pagès[1]*, Vassilis Kehayas[1,2], Daniela Baptista[1], Roberta Tatti[1,2], Alan Carleton[1] & Anthony Holtmaat[1]

Long-term synaptic potentiation (LTP) is thought to be a key process in cortical synaptic network plasticity and memory formation[1]. Hebbian forms of LTP depend on strong postsynaptic depolarization, which in many models is generated by action potentials that propagate back from the soma into dendrites[2,3]. However, local dendritic depolarization has been shown to mediate these forms of LTP as well[1,4,5]. As pyramidal cells in supragranular layers of the somatosensory cortex spike infrequently[6–8], it is unclear which of the two mechanisms prevails for those cells *in vivo*. Using whole-cell recordings in the mouse somatosensory cortex *in vivo*, we demonstrate that rhythmic sensory whisker stimulation efficiently induces synaptic LTP in layer 2/3 (L2/3) pyramidal cells in the absence of somatic spikes. The induction of LTP depended on the occurrence of NMDAR (*N*-methyl-D-aspartate receptor)-mediated long-lasting depolarizations, which bear similarities to dendritic plateau potentials[9–13]. In addition, we show that whisker stimuli recruit synaptic networks that originate from the posteromedial complex of the thalamus (POm). Photostimulation of channelrhodopsin-2 expressing POm neurons generated NMDAR-mediated plateau potentials, whereas the inhibition of POm activity during rhythmic whisker stimulation suppressed the generation of those potentials and prevented whisker-evoked LTP. Taken together, our data provide evidence for sensory-driven synaptic LTP *in vivo*, in the absence of somatic spiking. Instead, LTP is mediated by plateau potentials that are generated through the cooperative activity of lemniscal and paralemniscal synaptic circuitry[14–16].

In most cortical synaptic LTP studies *in vivo*, strong postsynaptic depolarization was provided by action-potential-triggering somatic current injections[3]. To examine whether sensory stimuli can elicit LTP of synaptic inputs on L2/3 pyramidal cells in the mouse somatosensory cortex without the help of artificially triggered backpropagating action potentials, we recorded sensory-evoked postsynaptic potentials (PSPs) in the barrel cortex *in vivo*, and applied a rhythmic whisker stimulation (RWS) protocol that has been shown to enhance whisker-evoked local field potentials[17]. Whole-cell patch recordings were targeted to cells above the C2 barrel of urethane-anaesthetized mice[6,18] (Fig. 1a). Using a piezoelectric actuator, the principal whisker was deflected back and forth (100-ms deflections) for 1 min at a frequency of 8 Hz, which is within the range of frequencies at which mice sample objects[15]. In all cells, RWS evoked a sustained subthreshold depolarization (Fig. 1a), which was reminiscent of an evoked, NMDAR-dependent, cortical upstate[19,20]. None of the recorded cells displayed somatic action potentials during RWS. On average, RWS elicited a significant potentiation of subsequent single (0.1 Hz) whisker-deflection-evoked short-latency PSP amplitudes (PSP_{short}; Fig. 1b, c; values for Figs 1–4 are provided in Supplementary Information). This LTP lasted for as long as the cells could be recorded from (at least 15 min after RWS), and correlated with the decay time of the sustained depolarization (Extended Data Fig. 1a, b). Pharmacological or hyperpolarization-mediated suppression of NMDAR conductance specifically attenuated the RWS-evoked sustained depolarization, and prevented LTP (Fig. 1d–i, Extended Data Fig. 1 and Supplementary Note 1). RWS-induced LTP remained specific to the rhythmically stimulated synaptic pathway (Extended Data Fig. 2 and Supplementary Note 2), increased gradually over a timescale of minutes, and was occluded upon a second RWS 10 min after the first stimulation (Extended Data Fig. 3a, b). RWS and hyperpolarization did not significantly alter intrinsic cell membrane properties, and small changes thereof did not correlate with the

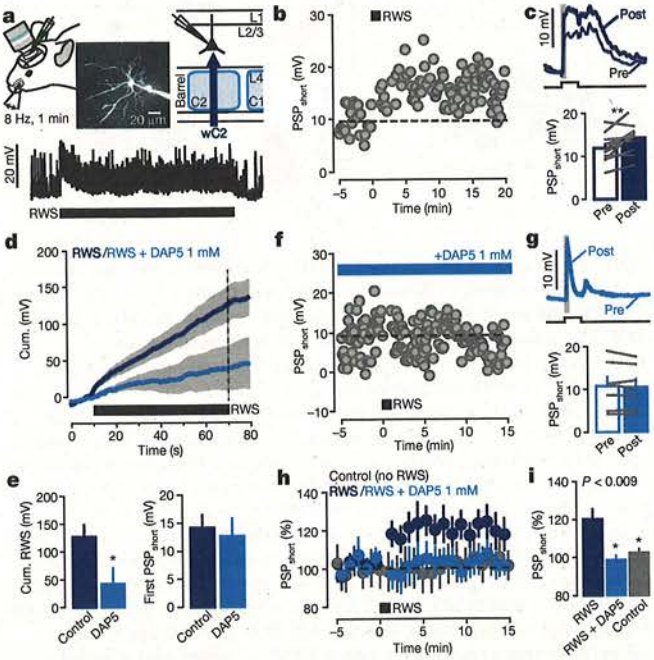

Figure 1 | Rhythmic whisker stimulation induces LTP in L2/3 neurons. **a**, Top, schematic of recordings in L2/3 cells *in vivo*. PSPs and RWS are evoked by the principal whisker (wC2). Bottom, example trace of sustained depolarization induced by RWS (8 Hz for 1 min; black bar). **b**, Single-cell whisker-evoked short latency PSP amplitudes (PSP_{short}; see **c**) before and after RWS. **c**, Top, single-cell averaged traces, pre and post RWS. Grey box, PSP_{short} window. Bottom, mean amplitudes, pre and post RWS ($n = 11$, $^{**}P = 0.008$). **d**, Cumulative RWS-induced depolarization. **e**, Mean cumulative depolarization at the end of RWS and amplitudes of the first PSP_{short} upon RWS (control, $n = 11$; +DAP5, $n = 7$; $P = 0.028$ (left) and $P = 0.703$ (right)). **f**, Single-cell whisker-evoked PSP_{short} amplitudes upon epidural DAP5 (1 mM). **g**, Top, single-cell averaged traces, pre and post RWS under DAP5. Bottom, mean amplitudes, pre and post RWS under DAP5 ($n = 7$, $P = 0.344$). **h**, Mean PSP_{short} amplitudes without RWS, and pre and post RWS in controls and under DAP5. **i**, Mean amplitudes normalized to baseline (RWS, $n = 11$; RWS +DAP5, $n = 7$; Control, $n = 7$; $P < 0.009$, one-way ANOVA; $^{*}P < 0.05$, post-hoc comparisons versus RWS control). Error bars, s.e.m; square pulse lines, whisker deflections (100 ms); grey lines between bars, pairs.

[1]Department of Basic Neurosciences and the Center for Neuroscience, CMU, University of Geneva, 1 rue Michel Servet, 1211 Geneva, Switzerland. [2]Lemanic Neuroscience Doctoral School, 1 rue Michel Servet, 1211 Geneva, Switzerland. †Present address: Institute for Interdisciplinary Neuroscience (IINS), UMR 5297 CNRS and University of Bordeaux, 146 rue Léo-Saignat, 33077 Bordeaux, France. *These authors contributed equally to this work.

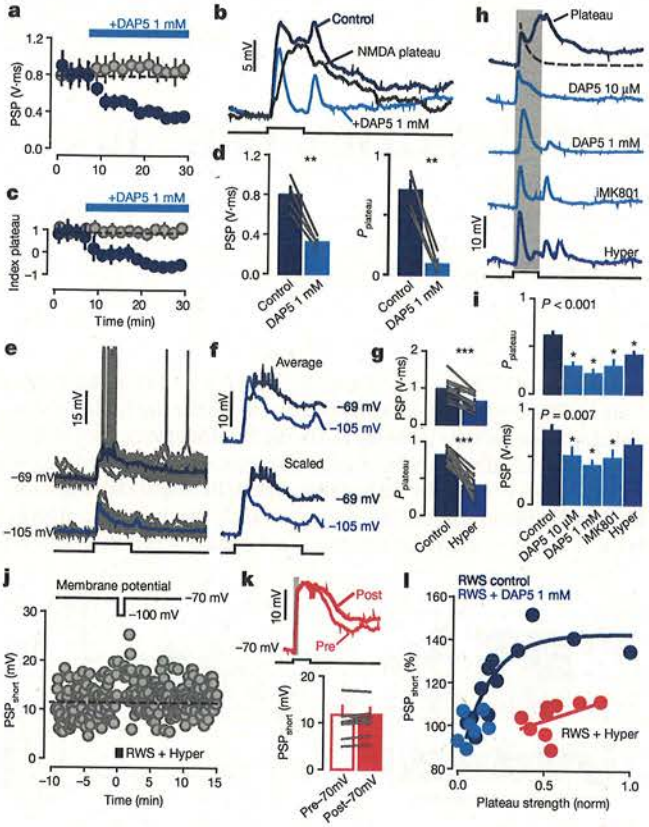

Figure 2 | Whisker deflections evoke NMDAR-mediated plateau potentials. **a**, Mean whisker-evoked 100-ms PSP integrals in controls (grey, $n = 7$), and upon epidural DAP5 (blue, $n = 5$). **b**, Single-cell averaged traces ($n = 40$ trials). NMDAR-mediated plateau: DAP5-trace subtracted from control trace. **c**, Mean $Index_{plateau}$ (see Extended Data Fig. 4) of same cells as in **a**. **d**, Mean PSP integrals and plateau probabilities ($n = 5$, $^{**}P = 0.004$ (left) and $^{**}P = 0.002$ (right)). **e**, Single-cell examples of responses at two different holding potentials (grey, single trials; blue, averaged traces). **f**, Top, averaged traces from **e**. Bottom, traces normalized to PSP_{short} in order to compensate for increased driving force, showing that hyperpolarization blocks the plateau. **g**, Mean PSP integrals and plateau probabilities ($n = 11$, $^{***}P < 0.001$). **h**, Single-cell averaged traces under control (dark blue) and various NMDAR conductance-reducing conditions. **i**, Comparison of mean plateau potential probabilities and integrals under various conditions (control, $n = 44$; 10 µM DAP5, $n = 9$; 1 mM DAP5, $n = 12$; iMK801, $n = 10$; Hyper, $n = 11$; $P < 0.001$ (top) and $P = 0.007$ (bottom), one-way ANOVA; $^{*}P < 0.05$, post-hoc comparisons versus control). **j**, Single-cell PSP_{short} amplitudes recorded at resting membrane potential (−70 mV) before and after RWS. The cell was hyperpolarized (−100 mV) during RWS. **k**, Top, single-cell averaged traces, pre and post RWS upon hyperpolarization. Grey box, PSP_{short} window. Bottom, mean amplitude, pre and post RWS recorded at −70 mV, but upon hyperpolarization during RWS ($n = 9$, $P = 0.993$). **l**, Normalized plateau strength predicts the level of RWS-induced LTP in controls (nonlinear regression; $R^2 = 0.76$, $P = 0.002$). DAP5 blocks plateaus and LTP. Neurons with high plateau strengths fail to potentiate when hyperpolarized during RWS (PSP_{short}, mean: 103.6 ± 6%, $n = 9$). Error bars, s.e.m; square pulse lines, whisker deflections (100 ms); grey lines between bars, pairs.

magnitude of LTP (Extended Data Fig. 3c–n). Together, the data indicate that RWS elicits bona fide synaptic LTP by evoking a cell autonomous and sustained NMDAR-dependent subthreshold depolarization.

We next investigated what may cause the sustained subthreshold depolarization upon RWS. In accordance with previous reports single whisker deflections typically evoked compound PSPs, containing short- and long-latency components, which is similar to the sparse, temporal, spiking profiles of L2/3 cells (Fig. 1c and Extended Data Fig. 4a, b)[6,21–23]. Short-latency PSPs were always present. Long-latency PSPs occurred with variable probabilities in different cells. They had an all-or-none, nonlinear appearance

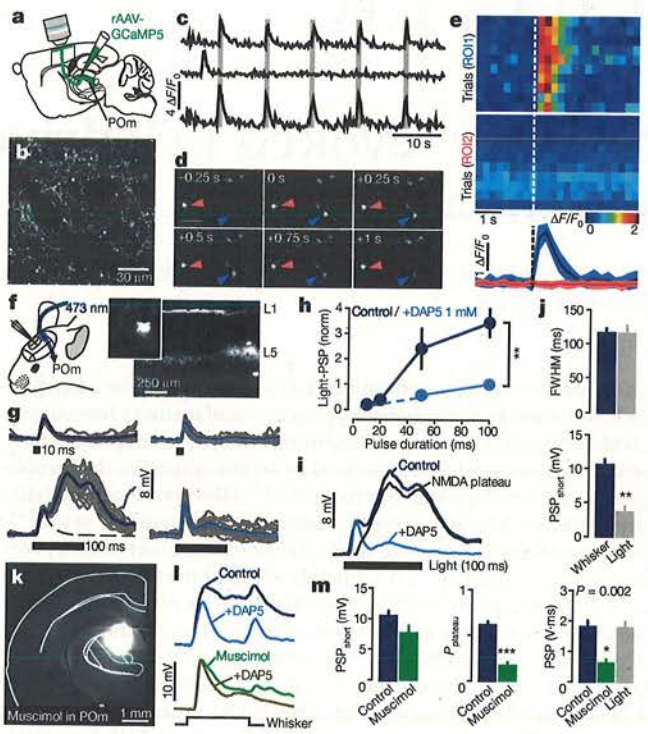

Figure 3 | Plateau potentials depend on POm activity. **a**, **b**, POm neurons were transfected with adeno-associated virus (AAV)-GCaMP5G and their axons were imaged in L1 of the barrel cortex (**b**). **c**, Example traces of Ca^{2+} signals ($\Delta F/F_0$) in POm axonal boutons upon whisker deflection bouts (5 at 20 Hz; grey lines). **d**, Example of a responsive (blue arrowhead) and an unresponsive (red arrowhead) axon. Scale bar, 5 µm. **e**, Top, whisker-evoked (dashed line) Ca^{2+} signals ($\Delta F/F_0$) in the boutons of **d** (rows, 10 successive trials). Bottom, mean whisker-evoked Ca^{2+} signals in the two boutons. **f**, Photostimulation of ChR2-expressing POm neurons using an optical fibre, and ChR2 expression profiles in the thalamus (inset) and cortex. **g**, Single-cell examples of photostimulus-evoked PSPs (in L2/3 cells) before (left) and after DAP5 (right). Grey, single trials; blue, averaged traces; black bar, photostimulus. **h**, Photostimulus-evoked PSP integrals as a function of stimulus duration (normalized to the maximal integral upon a 100-ms pulse +DAP5 (control, $n = 7$; DAP5, $n = 5$; $^{**}P = 0.002$)). **i**, Averaged 100-ms light-pulse-evoked PSPs from **g**. NMDA-plateau: DAP5-trace subtracted from control trace. **j**, Comparison of 100-ms light pulse-evoked and whisker-evoked PSPs (whisker, $n = 33$; light, $n = 11$; $P = 0.918$ (top); $^{**}P < 0.01$ (bottom)). **k**, Coronal brain section with fluorescent muscimol in the POm. **l**, Single-cell averaged traces of 100-ms whisker-evoked PSPs in controls and after POm inactivation, with and without DAP5. **m**, Effects of POm inactivation on PSP_{short} (control, $n = 33$; muscimol, $n = 9$; $P = 0.095$), plateau potential probabilities (control, $n = 44$; muscimol, $n = 9$; $^{***}P < 0.001$, Mann–Whitney U-test), and PSP integrals (over 300 ms; control, $n = 33$; muscimol, $n = 9$; 100 ms light, $n = 13$; $P = 0.002$, one-way ANOVA, and $^{*}P < 0.05$, post-hoc comparisons versus control). Error bars represent s.e.m.

and were selectively attenuated upon an NMDAR block (Fig. 2a–d and Extended Data Fig. 4a–g). This indicates that long-latency PSPs share similarities with plateau potentials[9–13]. We termed them accordingly. Importantly, plateau potentials, but not short-latency PSPs, were also significantly attenuated upon a cell-autonomous suppression of NMDAR conductance using artificial hyperpolarization (−100 mV), or intracellular MK801 (1 mM) (Fig. 2e–i and Extended Data Fig. 4g). Conversely, when holding the neurons at a slightly depolarized state, or in some occasions at resting states, these potentials evoked spikes (Fig. 2e). This suggests that whisker-evoked long-latency spiking under normal conditions is associated with the occurrence of NMDAR-dependent plateau potentials (Extended Data Fig. 4b)[10,13,21,24]. The occurrence of plateau potentials was not critically dependent on the 100-ms duration of the whisker deflections (Extended Data Fig. 4h–j).

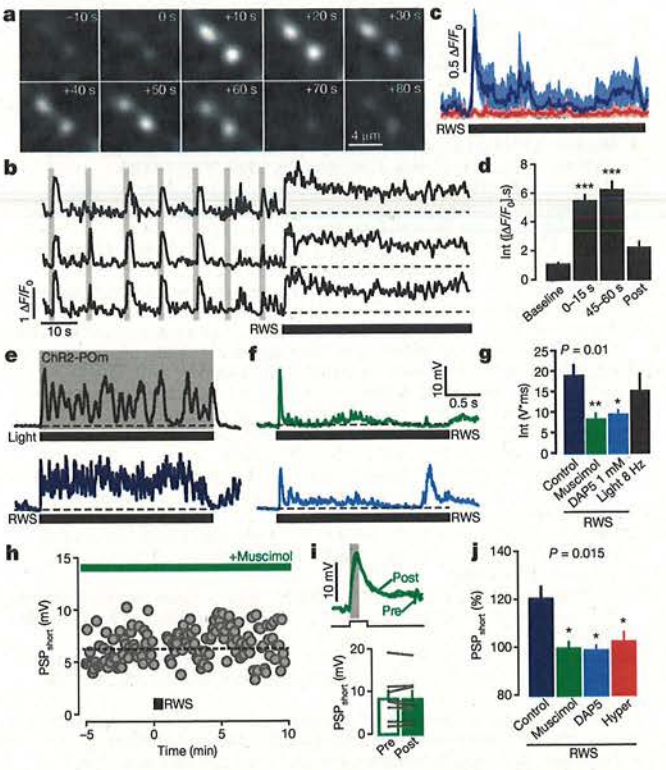

Figure 4 | RWS-evoked LTP depends on POm-mediated plateau potentials. **a**, Example of POm axonal bouton Ca^{2+} dynamics ($\Delta F/F_0$) upon RWS. **b**, Ca^{2+} signals in POm boutons upon whisker-deflection bouts (grey lines) and RWS. **c**, Mean RWS-induced Ca^{2+} signals in the 25 most active (blue) and least active (red) boutons (see Extended Data Fig. 6). Shaded area, s.d. **d**, Integrated responses before, during and after RWS ($n = 765$; $***P < 0.001$). **e**, Example of the membrane depolarization (L2/3 cell) upon rhythmic photostimulation of POm (20 flashes at 8 Hz) or RWS (20 stimuli at 8 Hz). Black bar, stimulus period. **f**, RWS-induced membrane depolarization upon muscimol-POm inactivation or DAP5. **g**, Mean integrated membrane potentials (over 2.5 s) (control, $n = 14$; muscimol, $n = 4$; DAP5, $n = 15$; light 8 Hz, $n = 5$; $P = 0.01$, one-way ANOVA; $*P < 0.05$ and $**P < 0.01$, post-hoc comparisons versus control). **h**, Single-cell whisker-evoked PSP_{short} amplitudes before and after RWS upon muscimol-mediated POm inactivation. **i**, Top, single-cell averaged traces, pre and post RWS. Grey line, PSP_{short} window. Square pulse line, whisker deflection (100 ms). Bottom, mean amplitudes pre and post RWS upon POm inactivation ($n = 9$, $P = 0.972$). Grey lines between bars, pairs. **j**, Comparison of normalized PSP_{short} amplitudes upon RWS in controls, and after a POm or NMDAR block (control, $n = 11$; muscimol, $n = 9$; DAP5, $n = 7$; Hyper, $n = 9$; $P = 0.015$, one-way ANOVA, and $*P < 0.05$, post-hoc comparisons versus control). Error bars, s.e.m.

NMDAR-mediated plateau potentials or summating NMDA spikes have been observed in various cell types in the somatosensory cortex *in vivo*[10,11,13], where they are characterized by local and spreading dendritic Ca^{2+} transients. We confirmed that under our conditions too, single whisker deflections evoke Ca^{2+} transients in spines and dendritic shafts, both under wakefulness (data not shown) and anaesthesia. Local and large-scale events occurred at various positions in the dendritic tree (Extended Data Fig. 5a–e and Supplementary Note 3). These responses were diminished upon an NMDAR block, and increased upon RWS (Extended Data Fig. 5f–j), similar to the plateau potentials and sustained depolarization in our whole-cell recordings. Together, this indicates that single-whisker-deflection-mediated plateaus and the RWS-mediated sustained depolarization in our recordings are likely to be supported by NMDAR-mediated dendritic Ca^{2+} events[10,11,13,25].

The plateau strength of neurons (that is, the product of the probability for a whisker deflection to elicit a plateau potential and the average integrated depolarization) correlated with the magnitude of RWS-induced LTP (Fig. 2l). Neurons bearing high plateau strengths could not be potentiated when they were hyperpolarized during RWS (Fig. 2j–l). This strongly suggests that the plateau potentials are essential for RWS-induced LTP.

Next, we questioned what could be the synaptic source of NMDAR-mediated plateau potentials. Previous studies indicate that in the somatosensory cortex they are generated by coincident activity of segregated excitatory synaptic pathways[10,11,13]. We reasoned that in anaesthetized mice plateau potentials may depend on co-activation of intracolumnar lemniscal and thalamocortical paralemniscal pathways[10,11]. Paralemniscal input to L2/3 cells may be directly or indirectly provided by thalamic POm efferents that target pyramidal cell dendrites in L5A and L1 (refs 14–16, 26–29). This system is involved in the kinematics of whisking[15] and may provide feedback information to pyramidal cells[16].

To test whether POm efferents are activated by passive whisker stimuli[15,28,29], we expressed the genetically encoded Ca^{2+} indicator GCaMP5G in POm neurons (Fig. 3a, b), and imaged responses in their projections to somatosensory cortex L1 through a cranial window. Whisker deflections evoked Ca^{2+} transients with various latencies in a substantial portion of the terminals in awake and anaesthetized mice (Fig. 3c–e and Extended Data Fig. 6). The shortest response times matched the latencies of the plateau potentials. Furthermore, the pattern of activation was widespread and did not remain limited to the whisker's home barrel column (Extended Data Fig. 7a–c and Supplementary Note 4). Interestingly, and in contrast to short-latency PSPs, the plateau potentials were not selective for the principal whisker, which supports the possibility that the POm thalamocortical circuitry is indeed involved in generating them (Extended Data Fig. 7d, e).

To test this directly we expressed the recombinant light-gated ion channel channelrhodopsin-2-Venus (ChR2-Venus) in the POm and recorded photostimulus-evoked PSPs in L2/3 cells (Fig. 3f, g and Extended Data Fig. 8a–c and Supplementary Note 5). POm neurons were stimulated using an optical fibre that was guided by a stereotactically implanted cannula (Fig. 3f). Short square light pulses (10–20 ms) produced small-amplitude PSPs, longer pulses (50–100 ms) produced plateaus (Fig. 3g–h). This indicates that a strong activation of POm thalamic nuclei may generate plateau potentials by itself, through monosynaptic inputs (Extended Data Fig. 8d, e and Supplementary note 5) or, more probably, through the large-scale recruitment of cortical paralemniscal synaptic networks that project to L2/3 cells[14,27,28]. This suggests that the POm-associated synaptic circuitry mediates whisker-evoked plateau potentials. Indeed, analogous to whisker-evoked plateaus, photostimulus-evoked plateaus were eliminated upon an NMDAR block (Fig. 3g, h). The full width at half maximum of the NMDAR-mediated plateaus was equal between whisker and 100-ms light stimuli (Fig. 3i, j; for example, compare with Fig. 2b). Importantly, for these photostimuli the peak amplitude of the short-latency PSPs was significantly lower than that of whisker-evoked PSPs (Fig. 3j), confirming that photostimuli did not generate plateau potentials through a large-scale recruitment of lemniscal synaptic pathways.

To test further the role of this paralemniscal circuitry, we specifically suppressed POm activity using the GABA-A-R selective agonist muscimol (Fig. 3k, Extended Data Fig. 9a and Supplementary Note 6). This did not affect whisker-evoked short-latency PSPs, but greatly reduced whisker-evoked plateau potential probabilities (Fig. 3l, m). The inhibition of POm activity was sufficient to eliminate most of the evoked NMDAR-mediated plateaus, since an additional NMDAR block did not further reduce them (Fig. 3l).

The role of the POm in the generation of plateau potentials suggests that it is also involved in the production of the RWS-evoked sustained depolarization. Indeed, RWS evoked sustained Ca^{2+} transients in a portion of POm-derived axonal boutons (Fig. 4a–d and Extended Data Fig. 6e, f). Rhythmic photostimulation of ChR2-expressing POm neurons evoked a sustained depolarization similar to RWS (Fig. 4e, g). Conversely, RWS failed to evoke a sustained depolarization upon muscimol-mediated suppression of POm activity, similar to the effect of DAP5 (Fig. 4f, g). This suggests that POm activity evokes multiple plateaus during RWS. To test the causal relationship between plateau potentials, RWS-evoked sustained

depolarization, and RWS-induced LTP without blocking NMDARs, we applied RWS to muscimol-injected mice. In these mice RWS failed to induce LTP (Fig. 4h, i), similar to the effect of suppressing NMDAR conductance (Fig. 4j). This strongly suggests that plateau potentials, driven by the co-activation of POm-associated synaptic circuitry facilitate whisker-evoked LTP.

In summary, our data provide evidence for sensory-evoked LTP that is independent of somatic spikes, displaying similarities to *in vitro* experiments in hippocampus[30]. *In vivo*, the occurrence of LTP in the absence of somatic spikes may be an important mechanism to strengthen synapses between weakly connected neurons, without the necessity for sensory inputs to first elicit a sufficient number of action potentials. Since L2/3 neurons in the somatosensory cortex normally spike sparsely or infrequently[8], this mechanism may also prevent neurons from losing synaptic input due to spike-timing-dependent long-term depression (LTD)-like processes[3].

We also found that sensory-evoked LTP may depend on paralemniscal synaptic inputs that originate from the POm of the thalamus. This circuitry provides contextual or predictive information for external sensory stimuli that feed forward through lemniscal pathways[16]. Our data suggest that the repeated coincident activity of this feedback circuitry may increase L2/3 neurons' sensitivity to future sensory stimuli. It is likely that during wakefulness dendritic plateau potentials that are mediated by inputs from motor cortex[11] also function to facilitate this—perhaps Hebbian—form of LTP (Supplementary Note 7).

Online Content Methods, along with any additional Extended Data display items and Source Data, are available in the online version of the paper; references unique to these sections appear only in the online paper.

Received 3 February; accepted 7 July 2014.
Published online 31 August 2014.

1. Bliss, T. V. P. & Collingridge, G. L. A synaptic model of memory: long-term potentiation in the hippocampus. *Nature* **361,** 31–39 (1993).
2. Markram, H., Luebke, J., Frotscher, M. & Sakmann, B. Regulation of synaptic efficacy by coincidence of postsynaptic APs and EPSPs. *Science* **275,** 213–215 (1997).
3. Feldman, D. E. The spike-timing dependence of plasticity. *Neuron* **75,** 556–571 (2012).
4. Golding, N. L., Staff, N. P. & Spruston, N. Dendritic spikes as a mechanism for cooperative long-term potentiation. *Nature* **418,** 326–331 (2002).
5. Lisman, J. & Spruston, N. Postsynaptic depolarization requirements for LTP and LTD: a critique of spike timing-dependent plasticity. *Nature Neurosci.* **8,** 839–841 (2005).
6. Brecht, M., Roth, A. & Sakmann, B. Dynamic receptive fields of reconstructed pyramidal cells in layers 3 and 2 of rat somatosensory barrel cortex. *J. Physiol. (Lond.)* **553,** 243–265 (2003).
7. Poulet, J. F. & Petersen, C. C. Internal brain state regulates membrane potential synchrony in barrel cortex of behaving mice. *Nature* **454,** 881–885 (2008).
8. O'Connor, D. H., Peron, S. P., Huber, D. & Svoboda, K. Neural activity in barrel cortex underlying vibrissa-based object localization in mice. *Neuron* **67,** 1048–1061 (2010).
9. Antic, S. D., Zhou, W. L., Moore, A. R., Short, S. M. & Ikonomu, K. D. The decade of the dendritic NMDA spike. *J. Neurosci. Res.* **88,** 2991–3001 (2010).
10. Lavzin, M., Rapoport, S., Polsky, A., Garion, L. & Schiller, J. Nonlinear dendritic processing determines angular tuning of barrel cortex neurons *in vivo*. *Nature* **490,** 397–401 (2012).
11. Xu, N. L. *et al.* Nonlinear dendritic integration of sensory and motor input during an active sensing task. *Nature* **492,** 247–251 (2012).
12. Major, G., Larkum, M. E. & Schiller, J. Active properties of neocortical pyramidal neuron dendrites. *Annu. Rev. Neurosci.* **36,** 1–24 (2013).
13. Palmer, L. M. *et al.* NMDA spikes enhance action potential generation during sensory input. *Nature Neurosci.* **17,** 383–390 (2014).
14. Bureau, I., von Saint Paul, F. & Svoboda, K. Interdigitated paralemniscal and lemniscal pathways in the mouse barrel cortex. *PLoS Biol.* **4,** e382 (2006).
15. Diamond, M. E., von Heimendahl, M., Knutsen, P. M., Kleinfeld, D. & Ahissar, E. 'Where' and 'what' in the whisker sensorimotor system. *Nature Rev. Neurosci.* **9,** 601–612 (2008).
16. Larkum, M. A cellular mechanism for cortical associations: an organizing principle for the cerebral cortex. *Trends Neurosci.* **36,** 141–151 (2013).
17. Megevand, P. *et al.* Long-term plasticity in mouse sensorimotor circuits after rhythmic whisker stimulation. *J. Neurosci.* **29,** 5326–5335 (2009).
18. Gambino, F. & Holtmaat, A. Spike-timing-dependent potentiation of sensory surround in the somatosensory cortex is facilitated by deprivation-mediated disinhibition. *Neuron* **75,** 490–502 (2012).
19. Poulet, J. F., Fernandez, L. M., Crochet, S. & Petersen, C. C. Thalamic control of cortical states. *Nature Neurosci.* **15,** 370–372 (2012).
20. Favero, M. & Castro-Alamancos, M. A. Synaptic cooperativity regulates persistent network activity in neocortex. *J. Neurosci.* **33,** 3151–3163 (2013).
21. Armstrong-James, M., Welker, E. & Callahan, C. A. The contribution of NMDA and non-NMDA receptors to fast and slow transmission of sensory information in the rat SI barrel cortex. *J. Neurosci.* **13,** 2149–2160 (1993).
22. Petersen, C. C., Grinvald, A. & Sakmann, B. Spatiotemporal dynamics of sensory responses in layer 2/3 of rat barrel cortex measured *in vivo* by voltage-sensitive dye imaging combined with whole-cell voltage recordings and neuron reconstructions. *J. Neurosci.* **23,** 1298–1309 (2003).
23. Wilent, W. B. & Contreras, D. Synaptic responses to whisker deflections in rat barrel cortex as a function of cortical layer and stimulus intensity. *J. Neurosci.* **24,** 3985–3998 (2004).
24. Rema, V., Armstrong-James, M. & Ebner, F. F. Experience-dependent plasticity of adult rat S1 cortex requires local NMDA receptor activation. *J. Neurosci.* **18,** 10196–10206 (1998).
25. Grienberger, C., Chen, X. & Konnerth, A. NMDA receptor-dependent multidendrite Ca^{2+} spikes required for hippocampal burst firing *in vivo*. *Neuron* **81,** 1274–1281 (2014).
26. Deschênes, M., Veinante, P. & Zhang, Z. W. The organization of corticothalamic projections: reciprocity versus parity. *Brain Res. Brain Res. Rev.* **28,** 286–308 (1998).
27. Petreanu, L., Mao, T., Sternson, S. M. & Svoboda, K. The subcellular organization of neocortical excitatory connections. *Nature* **457,** 1142–1145 (2009).
28. Feldmeyer, D. Excitatory neuronal connectivity in the barrel cortex. *Front. Neuroanat.* **6,** 24 (2012).
29. Diamond, M. E., Armstrong-James, M., Budway, M. J. & Ebner, F. F. Somatic sensory responses in the rostral sector of the posterior group (POm) and in the ventral posterior medial nucleus (VPM) of the rat thalamus: dependence on the barrel field cortex. *J. Comp. Neurol.* **319,** 66–84 (1992).
30. Hardie, J. & Spruston, N. Synaptic depolarization is more effective than back-propagating action potentials during induction of associative long-term potentiation in hippocampal pyramidal neurons. *J. Neurosci.* **29,** 3233–3241 (2009).

Supplementary Information is available in the online version of the paper.

Acknowledgements We thank E. Ahissar and T. Oram for advice on the muscimol experiments. We appreciate C. Lüscher's comments on our manuscript. We thank L. L. Looger and D. Kim of the GENIE project, and K. Svoboda at the Janelia Farm Research Campus (HHMI) for distributing the GCaMP5G, GCaMP6S and ChR2 vectors, respectively. This work was supported by the Swiss National Science Foundation (grants 31003A_120685, 31003A_135631 and CRSI33_127289 to A.H.; 31003A_153410 to A.C.), the National Centre of Competence in Research (NCCR) SYNAPSY financed by the Swiss National Science Foundation (51AU40_125759), the International Foundation for Research on Paraplegia, and the Hans Wilsdorf Foundation. V.K. was supported by SyMBaD (EU FP7-PEOPLE-ITN Marie Curie, grant 238608).

Author Contributions F.G. performed the *in vivo* electrophysiology experiments; S.P. performed the Ca^{2+} imaging experiments; V.K. and F.G. performed the photostimulation experiments; D.B. and V.K. performed thalamocortical projection analyses; R.T. and F.G. performed *in vitro* electrophysiology experiments; A.C. and A.H. provided equipment and technical expertise; F.G., S.P., V.K. and A.H. conceived the studies; A.H. supervised the research; A.H., F.G. and S.P. wrote the manuscript with help from V.K.

Author Information Reprints and permissions information is available at www.nature.com/reprints. The authors declare no competing financial interests. Readers are welcome to comment on the online version of the paper. Correspondence and requests for materials should be addressed to A.H. (anthony.holtmaat@unige.ch).

METHODS

All procedures were carried out in accordance with protocols approved by the ethics committee of the University of Geneva and the authorities of the Canton of Geneva.

Surgery and intrinsic optical imaging. Three- to four-week-old male C57BL/6 mice were used. Anaesthesia was induced using isoflurane (4% with ~0.5 l min^{-1} O_2) and then continued using an intraperitoneal (i.p.) injection of urethane (1.5 g kg^{-1}, in lactated ringer solution containing (in mM) 102 NaCl, 28 Na-L-lactate, 4 KCl, 1.5 $CaCl_2$). Body temperature was maintained at 37 °C by a feedback-controlled heating pad (FHC). Eye ointment was applied to prevent dehydration. In accordance with Swiss Federal laws, analgesia was provided by local application of lidocaine (1%) and i.p. injection of buprenorphine (Temgesic, 0.05 mg kg^{-1}). The skin was disinfected with ethanol 70% and betadine, and a custom-made plastic chamber was attached to the skull above the barrel cortex using dental acrylic and dental cement (Jet Repair Acrylic, Lang Dental Manufacturing). The chamber was filled with sterile cortex buffer (in mM: 125 NaCl, 5 KCl, 10 glucose, 10 HEPES, 2 $CaCl_2$ and 2 $MgSO_4$ (pH 7.4)) and sealed with a glass coverslip.

Intrinsic optical signals were imaged as described previously[18], through the intact skull using a light guide system with a 700-nm (bandwidth of 20 nm) interference filter and a stable 100-W halogen light source. An image of the surface vascular pattern was taken using green light (546-nm interference filter) at the end of each imaging session. Images were acquired using the Imager 3001F (Optical Imaging, Mountainside, NJ) equipped with a large spatial 256 × 256 array, fast readout, and low read noise charge-coupled device (CCD) camera. The size of imaged area was adjusted by using a combination of two lenses with different focal distances (Nikon 50 mm, bottom lens, 135 mm, upper lens, f2.0; total magnification 2.7). The CCD camera was focused on a plane 300 μm below the skull surface. Responses were visualized by dividing the stimulus signal by the baseline signal, using the built-in Imager 3001F analysis program (Optical Imaging, Mountainside, NJ). Signals were analysed further using a custom routine in Matlab as described previously[18].

***In vivo* whole-cell recordings.** After imaging, adequate anaesthesia was assessed (absence of toe pinch reflexes, corneal reflexes, and vibrissae movements) and prolonged by supplementary urethane (0.15 g kg^{-1}, i.p.) if necessary. A small ~1 × 1 mm craniotomy (centred above the C2 whisker maximum intrinsic optical signal response) was made using a pneumatic dental drill. The dura was left intact. Whole-cell patch-clamp recordings of L2/3 pyramidal neurons were obtained as described previously[18,31]. High positive pressure (200–300 mbar) was applied to the pipette (5–8 MΩ) to prevent tip occlusion. After passing the pia the positive pressure was immediately reduced to prevent cortical damage. The pipette was then advanced in 1-μm steps, and pipette resistance was monitored in the conventional voltage clamp configuration. When the pipette resistance suddenly increased, positive pressure was relieved to obtain a 3–5-GΩ seal. After break-in, Vm was measured, and dialysis was allowed to occur for at least 5 min before deflecting the whisker. Data were acquired using a Multiclamp 700B Amplifier (Molecular Devices), and digitized at 10 kHz (National Instruments), using Matlab-based Ephus software (http://research.janelia.org/labs/display/ephus; The Janelia Farm Research Center). Offline analysis was performed using custom routines written in IGOR Pro (WaveMetrics).

Current-clamp recordings were made using a potassium-based internal solution (in mM: 135 potassium gluconate, 4 KCl, 10 HEPES, 10 Na2-phosphocreatine, 4 Mg-ATP, 0.3 Na-GTP and 25 μM AlexaFluor 488 hydrazide (Invitrogen), pH adjusted to 7.25 with KOH, 285 mOsM). Series and input resistance were monitored with a 100-ms long-lasting hyperpolarizing square pulse 400 ms before each whisker deflection and extracted offline by using a double-exponential fit. Recordings were discarded if the change in these parameters was larger than 30%. The bridge was usually not balanced, and liquid junction potential was not corrected. Traces were analysed as described previously[18]. For the action-potential analysis in Extended Data Fig. 3, action potentials were time-aligned to their respective threshold. The action-potential threshold was computed as the minimal membrane potential value at the time corresponding to the peak of the third derivative of the membrane potential, similar to methods described previously[32].

PSPs were evoked by back and forth deflection of the whisker (100 ms, 0.133 Hz) using a glass capillary 4 mm away from the skin attached to a piezoelectric ceramic actuators (PL-series PICMA, Physik Instrumente). The voltage applied to the actuator was set to evoke a whisker displacement of 0.6 mm with a ramp of 7–8 ms (for details see ref. 18). The C1 and C2 whiskers were independently deflected by different piezoelectric elements.

DAP5 (1 mM or 10 μM, Tocris) was topically applied to the dura mater, either prior or during the whole-cell recordings. Epidural application of 0.1–1 mM DAP5 has been shown to leave spiking in the thalamus intact and only minimally impact cortical L4 after 6 h of superfusion; 10 μM is entirely ineffective in suppressing spikes in L4 (ref. 24). MK-801 (1 mM, Tocris) was included in the internal solution. After break-in we waited for at least 5 min to let MK-801 diffuse into the cells. Typically, the effects of MK-801 became visible over the time course of 4–5 min, and remained stable thereafter. This indicates that the effects were largely due to cell autonomous blockage of NMDARs[10].

Injection of fluorescent muscimol into the POm. Mice were anaesthetized as described above. Analgesia was provided by local application of lidocaine and an i.p. injection of buprenorphine. A burr hole was made to stereotactically inject fluorescent muscimol (Bodipy-TMR-X, 500 μM in cortex buffer with 5% DMSO, Invitrogen) in the POm. The caudal sector of the POm that mainly projects to L1 of S1 (ref. 33) was specifically targeted using the following stereotaxic coordinates: rostrocaudal (RC), −2.00 mm; mediolateral (ML), −1.20 mm; dorsoventral (DV), −3.00 mm from the bregma (Extended Data Fig. 9). Glass pipettes (Wiretrol, Drummond) were pulled, back-filled with mineral oil, and front-loaded with the muscimol solution (100–150 nl were delivered (20 nl min^{-1}) using an oil hydraulic manipulator system (MMO-220A, Narishige)). For controls, the same volume of fluorescent muscimol was injected in thalamic structures that are not directly involved in somatosensory processing (Extended Data Fig. 9). The craniotomy was then covered with Kwik-Cast (WPI) and mice were prepared for intrinsic optical imaging and whole-cell recordings as described above. To achieve a maximal suppression of neuronal activity, patch-clamp recordings were performed at least one hour but no longer than 4 h after the injection. After completion of the experiment, mice were transcardially perfused with 4% paraformaldehyde in PBS (PFA), their brains extracted and post-fixed in PFA overnight. Coronal brain sections (100 μm) were made to confirm the site and spread of injections (Extended Data Fig. 9).

Virus injections and cranial windows. For virus injections we used either pups between postnatal days 12 and 15 (P12–P15) or adults (>4 weeks). In adults, anaesthesia was induced using isoflurane (4% with ~0.5 l min^{-1} O_2) and then continued using an i.p. injection of a mixture containing medetomidin (Dorbene, 0.2 mg kg^{-1}), midazolam (Dormicum, 5 mg kg^{-1}) and fentanyl (Duragesic, 0.05 mg kg^{-1}) in sterile NaCl 0.9% (MMF-mix). To prevent potential inflammation, salivary excretions or bradycardia, carprofenum (Rimadyl, 5 mg kg^{-1}) and glycopyrrolate (Robinul, 0.01 mg kg^{-1}) were injected subcutaneously (s.c.) before the surgery. Pups were injected under isoflurane anaesthesia. Mice were placed in a stereotaxic frame, the skin was disinfected with ethanol 70% and betadine, an incision was made, and 1% lidocaine was topically applied to the wound edges for additional local anaesthesia. The bregma and lambda were horizontally aligned. A burr hole was made using a pneumatic dental drill. Injections were targeted to the caudal part of the POm (coordinates from bregma: RC, −2.20 mm; ML, −1.20 mm; DV, −3.00 mm for adults; RC, −1.45 mm; ML, −1.60 mm; DV, −2.90 mm for pups)[27]. AAV2/1-CAG-ChR2-Venus (200–500 nl for adults; 50 nl for pups; 1.5 × 10^{12} GC, UNC Vector Core; based on the pACAGW-ChR2-Venus-AAV plasmid, Svoboda laboratory, Janelia Farm Research Center)[27,34] or 250–400 nl of AAV2/1-hSynap-GCaMP5G-WPRE-SV40 (2.13 × 10^{13} GC, Penn Vector Core and the GENIE project)[35] were injected at a maximum rate of 100 nl min^{-1} using a glass pipette (Wiretrol, Drummond) attached to an oil hydraulic manipulator (MMO-220A, Narishige). The solution was allowed to diffuse for at least 10 min before the pipette was withdrawn. The craniotomy was filled with Kwik-Cast (WPI) and the skin was re-attached with stainless steel staples (Precise DS15, 3M) or, in the case of AAV-GCaMP injections, a glass window was sealed into the craniotomy as previously described[36]. For cortical GCaMP expression, 20 nl of a mixture of AAV2/9-syn.Flex-GCaMP6 s-WPRE-SV40 (1.35 × 10^{13} GC ml^{-1}; Penn Vector Core and the GENIE project)[37] and AAV2/1-hSyn-Cre-WPRE-hGH (1.04x10^{13} GC ml^{-1}; Penn Vector Core) (15,000:1) were injected at a maximum rate of 10 nl min^{-1} just before sealing the window. The anaesthesia was reversed with an s.c. injection of a mixture containing atipamezole (Alzane, 2.5 mg kg^{-1}), flumazenil (Anexate, 0.5 mg kg^{-1}), and buprenorphine (Temgesic, 0.1 mg kg^{-1}) in sterile NaCl 0.9% (AFB-mix).

Cannulation and *in vivo* photostimulation. At least 2 weeks after the injection of AAV2-ChR2, mice were anaesthetized with MMF-mix. Intrinsic signal optical imaging was performed as above. A 21-gauge cannula (PlasticsOne) with 2.9 mm of exposed tip was stereotactically inserted through a burr hole (RC, −2.20 mm; ML, −1.20 mm; DV, −3.00 mm from bregma) and secured in place with dental cement (Jet Repair Acrylic, Lang Dental Manufacturing). The cannula was closed using a screw cap, and anaesthesia was reversed using AFB-mix. Mice were allowed to recover for 1 day before being prepared for *in vivo* patch-clamp recordings.

For the *in vivo* photostimulation of ChR2-expressing POm neurons, a stripped multimode optical fibre (BFL37-200, Thorlabs) fused to an internal guide (PlasticsOne) was inserted into the cannula. The fibre was coupled to a blue DPSS laser (SDL-473-050MFL, Shanghai Dream Lasers Technology), which was triggered by a pulse-stimulator (Master-8, A.M.P.I). The rise time of a 1-ms laser pulse (300 μs) was determined with a high-speed Si photodetector (DET10A, Thorlabs) coupled to an oscilloscope. The power output of the pulses was ~70% of the steady-state power. The steady-state power at the tip of the fibre was measured using a power meter (PM100D, S120C, Thorlabs) and adjusted before every recording session to ~40 mW mm^{-2}. No significant reduction in power was observed at the end of the experiments.

Ca^{2+} imaging and image analysis. A custom-made stainless steel post was cemented to the skull with dental acrylic (Jet Repair Acrylic, Lang Dental Manufacturing). Imaging was performed 14 to 30 days after virus injection using a custom-built 2-photon laser scanning microscope (https://openwiki.janelia.org/wiki/display/shareddesigns/Shared+Two-photon+Microscope+Designs), and using the custom-developed acquisition and microscope control software package ScanImage[38] (https://openwiki.janelia.org/wiki/display/ephus/ScanImage)[36]. For imaging of awake mice, mice were trained and habituated to the microscope setup for 7 days before the experiment. During imaging the mice were monitored using an infrared sensitive camera. The GCaMPs were excited using a Ti:sapphire laser (Coherent) tuned to $\lambda = 910$ nm. For detection we used GaAsP photomultiplier tubes (10770PB-40, Hamamatsu) and a ×20 (0.8 NA) microscope objective (Olympus). For imaging of axons the field of view typically spanned 300 × 300 μm (256 lines, 1 ms per line); for dendrites 43 μm × 21 – 43 μm (64 lines, 0.5 ms per line). The average excitation power was kept below 40 mW, as measured at the focal point of the objective. Bleaching of GCaMPs was negligible. Episodes in which piezo-mediated whisker deflections were immediately followed by active whisking were excluded from the analysis.

All image analyses were performed using custom routines in Matlab. We used cross-correlation based on rigid body translation to register images over time. Small regions of interest (ROIs) were drawn in the dendritic shafts (~1 μm^2) or around axonal boutons (~7 μm^2), based on averaged and standard deviation images. For each ROI the baseline fluorescence (F_0) was calculated based on the mean fluorescence intensity within the selected ROI, averaged over 100 consecutive frames before whisker stimulation. Change in fluorescence ($\Delta F_t/F_0$) was defined as $(F_t - F_0)/F_0$, were F_t is the fluorescence intensity at time t ($t \triangleq$ time of the first pixel in each frame). Boutons were imaged at a depth of 18 μm to 42 μm below the pia, dendrites between 18 μm and 70 μm. The onset of the response was defined as the time in between the whisker stimulus trigger and the time point at which fluorescence intensity reached a 2× baseline standard deviation threshold ($F_0 + (2 \times$ s.d.)). For extracting spatial and temporal properties of dendritic Ca^{2+} events (Extended Data Fig. 5) a Gaussian function was fitted to the fluorescence intensities of the ROIs in a visually 'active' region. All Gaussian fits were normalized to their maximum value. The time course of the change in fluorescence was extracted from the ROI that represented the peak of the Gaussian. A region was considered to be responsive if the fluorescence intensity remained above the threshold ($F_0 + (2 \times$ s.d.)) for at least three imaging frames.

To evaluate the ChR2-Venus expression profiles and the spread of fluorescent mucimol (Extended Data Figs 8 and 9), wide-field epifluorescence images were taken of fixed brain slices. Illumination was set such that the full dynamic range of the 16-bit images was used. A threshold was applied using Fiji's[39] implementation of the Kapur-Sahoo-Wong (Maximum Entropy) method[40]. The resulting image masks were registered to the corresponding coronal plates (ranging from −1.94 to −2.70 mm) of the Paxinos mouse brain atlas[41] using Photoshop (Adobe), at various distances posterior to bregma.

***In vitro* whole-cell recordings.** Coronal slices (thickness = 350 μm) were cut with a vibratome (Leica VT S1000) in ice-cold cutting solution containing (in mM): 83 NaCl, 2.5 KCl, 0.5 $CaCl_2$, 3.3 $MgSO_4$, 26.2 $NaHCO_3$, 1 NaH_2PO_4, 22 D-glucose and 72 sucrose. Slices were transferred in normal ACSF at ~34 °C for about 30 min and stored at room temperature before the experiment. ACSF contained (in mM): 124 NaCl, 3 KCl, 2 $CaCl_2$, 1.3 $MgSO_4$, 26 $NaHCO_3$, 1.25 NaH_2PO_4, 10 D-glucose with osmolarity of 300 mOsm and pH 7.3 when bubbled with 95% O_2 + 5% CO_2. Individual slices were transferred to the recording chamber and perfused with oxygenated ACSF. All recordings were performed at 37 °C (± 0.5 °C). Whole-cell recordings were performed using an IR-DIC microscope (Olympus BX51). Recordings were performed using borosilicate glass pipettes with resistance of 4–8 MΩ and filled with an intracellular solution containing (in mM): 110 K-gluconate, 10 KCl, 10 HEPES, 4 ATP, 0.3 GTP, 10 phosphocreatine and 0.4% biocytin. Recordings were amplified using Multiclamp 700 A amplifiers (Molecular devices, USA), filtered at 4 KHz, digitized (5–20 KHz), and acquired using PulseQ electrophysiology package running on Igor Pro (Wavemetrics, USA). Data processing and analysis was done using Igor (Wavemetrics) and Excel (Microsoft Office). For optogenetic experiments, axons terminals were stimulated with a LED (Thorlabs, Germany) that was focused around the recording electrode using a 4x microscope objective. Drugs used include 4-AP (100 μM; Sigma Aldrich) and tetrodotoxin (TTX) (1 μM; Latoxan). To confirm the identity of recorded neurons, 1 mM Alexa 568 hydrazide (Invitrogen) was added to the intracellular solution.

Statistical analysis. All statistics were performed using Matlab. The α significant level was set at 0.05. Normality of all value distributions was assessed by Shapiro–Wilk test ($\alpha = 0.05$). Equality of variance between different distributions was assessed by the Levene median test ($\alpha = 0.05$). Standard parametric tests were only used when data passed the normality and equal variance tests ($P > 0.05$). Non-parametric tests were used otherwise. Only two-sided tests were used. Randomization and blinding methods were not used. No statistical methods were used to estimate sample size, but β-power values were calculated and are provided in Supplementary Information, or in the Extended Data Figure legends.

31. Kitamura, K., Judkewitz, B., Kano, M., Denk, W. & Hausser, M. Targeted patch-clamp recordings and single-cell electroporation of unlabeled neurons *in vivo*. *Nature Methods* **5,** 61–67 (2008).
32. Kole, M. H. & Stuart, G. J. Is action potential threshold lowest in the axon? *Nature Neurosci.* **11,** 1253–1255 (2008).
33. Ohno, S. *et al.* A morphological analysis of thalamocortical axon fibers of rat posterior thalamic nuclei: a single neuron tracing study with viral vectors. *Cereb. Cortex* **22,** 2840–2857 (2012).
34. Zhang, F., Wang, L. P., Boyden, E. S. & Deisseroth, K. Channelrhodopsin-2 and optical control of excitable cells. *Nature Methods* **3,** 785–792 (2006).
35. Akerboom, J. *et al.* Optimization of a GCaMP calcium indicator for neural activity imaging. *J. Neurosci.* **32,** 13819–13840 (2012).
36. Holtmaat, A. *et al.* Long-term, high-resolution imaging in the mouse neocortex through a chronic cranial window. *Nature protocols* **4,** 1128–1144 (2009).
37. Chen, T. W. *et al.* Ultrasensitive fluorescent proteins for imaging neuronal activity. *Nature* **499,** 295–300 (2013).
38. Pologruto, T. A., Sabatini, B. L. & Svoboda, K. ScanImage: Flexible software for operating laser-scanning microscopes. *Biomed. Eng. Online* **2,** 13 (2003).
39. Schindelin, J. *et al.* Fiji: an open-source platform for biological-image analysis. *Nature Methods* **9,** 676–682 (2012).
40. Kapur, J. N., Sahoo, P. K. & Wong, A. K. C. A new method for gray-level picture thresholding using the entropy of the histogram. *Computer Vis. Graph. Image Process.* **29,** 273–285 (1985).
41. Paxinos, G. & Franklin, K. B. J. *The Mouse Brain in Stereotaxic Coordinates*. 2nd edn (Academic Press, 2001).

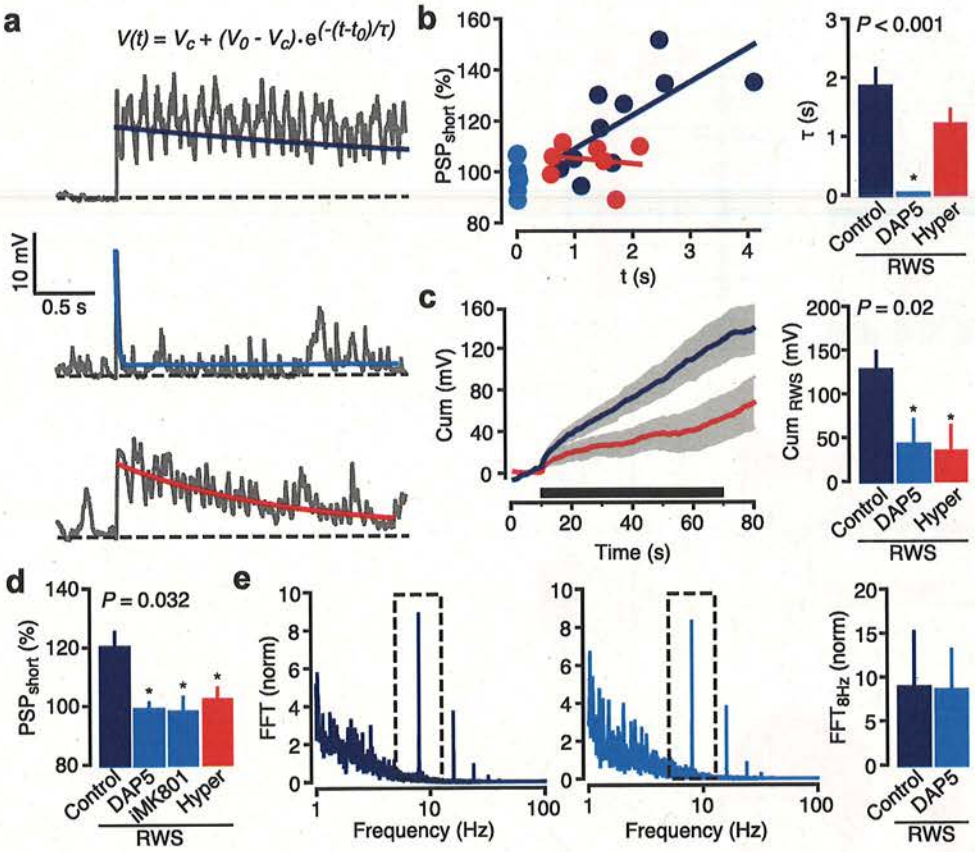

Extended Data Figure 1 | An NMDAR block suppresses RWS-induced sustained depolarization and prevents LTP. **a**, Examples of the postsynaptic depolarization as induced by RWS in controls (top), following a blockade of NMDARs by DAP5 (middle), and hyperpolarization (bottom). Only the first 2.5 s (20 deflections) of the recordings are shown. Responses were fit with an exponential, in which $V(t)$ is the depolarization at time point t in seconds, Vc is the depolarization constant (for example, reached after >10 s RWS), V_0 and t_0 are the depolarization and time at RWS onset, and τ is the time constant. **b**, Left, under control conditions (dark blue), the level of LTP is linearly correlated to the time constant (τ) of the exponential decay ($R^2 = 0.49$, $P < 0.05$). Following a suppression of NMDAR conductances the time constant and the percentage of LTP are independent (DAP5, light blue, $R^2 = 0.03$, $P > 0.05$; Hyper, red, $R^2 = 0.03$, $P > 0.05$). Each circle represents a single cell. Right, DAP5 significantly reduced the time constant (τ) of the exponential decay ($P < 0.001$; Kruskal–Wallis one-way ANOVA on ranks. $^*P < 0.05$, post-hoc Dunn's comparisons versus control condition). **c**, Left, the sustained depolarization during RWS is altered when NMDAR conductances are suppressed by hyperpolarization (red). Black bar indicates the RWS period. Right, cumulative depolarization at the end of the RWS period (control, 127 ± 21 mV, $n = 11$; +DAP5, 41 ± 28 mV, $n = 7$; Hyper, 34 ± 25 mV, $n = 9$; $P = 0.02$, one-way ANOVA ($\beta = 0.62$) and $^*P < 0.05$, post-hoc Holm-Sidak comparisons versus control condition). **d**, RWS failed to induce LTP when NMDARs are blocked by extracellular application of DAP5, when MK801 is included in the patch pipette, and when cells are hyperpolarized (control, 119.8 ± 6%, $n = 11$; DAP5, 98.7 ± 2.5, $n = 7$; iMK801, 98 ± 5%, $n = 3$; Hyper, 103.6 ± 6%, $n = 9$; $P = 0.032$, one-way ANOVA and $^*P < 0.05$, post-hoc Holm-Sidak comparisons versus control condition). **e**, A fast Fourier transform (FFT) of the responses during RWS (1 min), in controls (left) and after DAP5 application (middle). The FFT is normalized to the average FFT between 0.1 and 1 Hz. The presence of a strong 8 Hz component after DAP5 indicates that RWS-mediated inputs remain to be activated after the NMDAR block. Right, the magnitude of normalized FFT at 8 Hz is similar between control +DAP5 conditions (control, 8.8 ± 8.5, $n = 11$; +DAP5, 6.3 ± 4.6, $n = 7$; $P = 0.733$, Mann–Whitney U-test) confirming that part of the whisker deflection-evoked synaptic input was unaffected by DAP5, and follows the rhythmic stimulation. Values in **b**–**e** are represented as the mean ± s.e.m.

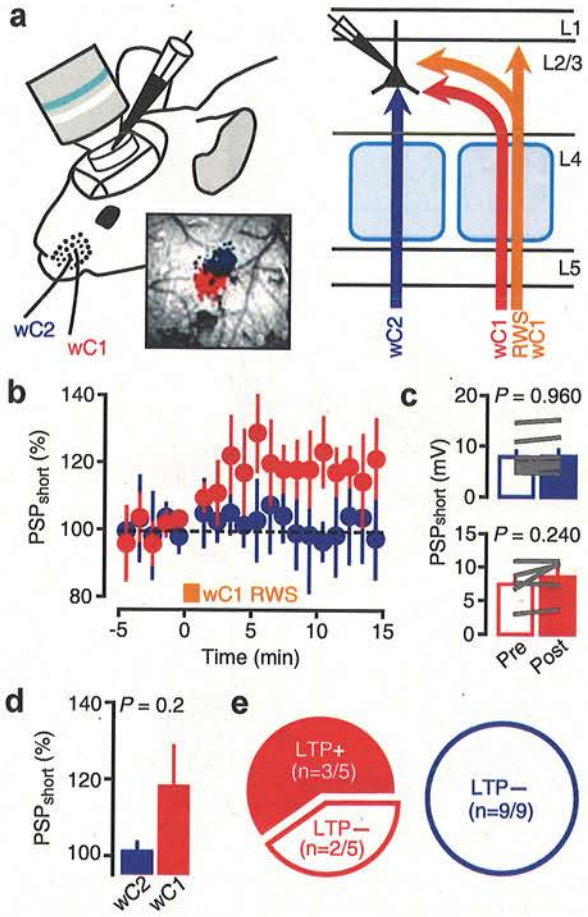

Extended Data Figure 2 | RWS-induced LTP is column- and whisker-specific. **a**, Left, schematic of the experiment: whole cell recordings are targeted to the C2 barrel column. Responses are recorded upon deflection of the C2 (principal whisker, wC2) or C1 (surrounding whisker, wC1) whisker. Inset, C2 (blue) and C1 (red) barrel-related columns were mapped using intrinsic optical imaging. Right, schematic of PW and SW-associated synaptic pathways projecting to L2/3 pyramidal cells. After RWS of wC1 (orange), single-whisker deflection PSPs were evoked either by the same whisker that was used for RWS (wC1, red) or by the neighbouring whisker (wC2, blue). **b**, Time course of mean wC2- (blue) and wC1-evoked (red) PSP_{short} amplitudes (± s.e.m.) following RWS of wC1 (orange bar). **c**, Mean PSP_{short} amplitude (± s.e.m.) before and after RWS. Top, wC1-RWS did not significantly enhance wC2-evoked mean PSP_{short} amplitudes (Pre, 7.8 ± 1.1 mV; Post, 7.9 ± 1.3 mV; $n = 8$; $P = 0.960$, paired t-test ($\beta = 0.05$)). Bottom, wC1-evoked amplitudes were enhanced in some cells, but despite this positive trend the average difference was not significant (Pre, 7.4 ± 1.3 mV; Post, 8.6 ± 1.3 mV; $n = 5$; $P = 0.240$, paired t-test ($\beta = 0.15$)). Grey lines indicate pairs. **d**, **e**, Although the average PSP amplitude as evoked by wC1 was not significantly different from wC2 (wC2, 101 ± 2.5%, $n = 8$; wC1, 118 ± 10%, $n = 5$; $P = 0.2$, Mann–Whitney U-test; **d**), the number of significantly potentiated cells was higher for wC1 (3 out of 5) than for wC2 (0 out of 9; **e**).

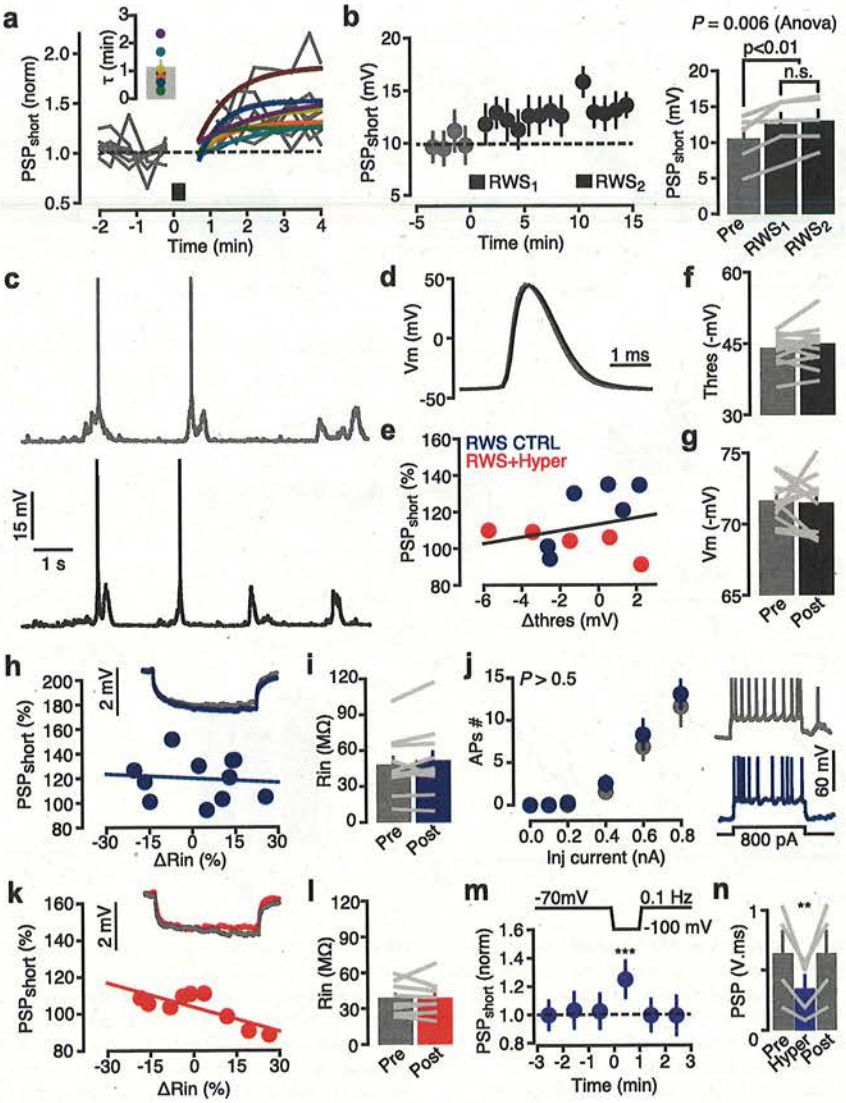

Extended Data Figure 3 | Characterization of RWS-induced LTP and stability of cell membrane properties. **a**, For each potentiated cell, a single exponential was fit to the normalized PSP_{short} amplitudes immediately following RWS, using the following equation: $PSP(t) = (1 + \Delta PSP_{LTP}) - (\Delta PSP_{LTP} \cdot e^{-(t/\tau)})$, in which $PSP(t)$ is the normalized PSP amplitude at time t in minutes, ΔPSP_{LTP} is the average change in PSP amplitude during the LTP phase, and τ the time constant (mean $\tau = 1.09 \pm 0.26$ min; range 0.3–2.34 min; $n = 7$). **b**, Left, time course of mean PSP_{short} amplitudes following two consecutive RWS protocols (RWS1 and RWS2). Right, the mean PSPshort amplitude increases upon RWS1 but does not further increase upon RWS2, indicating that RWS-evoked LTP is occluded (Pre, 10.32 ± 1.6 mV; RWS1, 12.35 ± 1.6 mV; RWS2, 12.98 ± 1.5 mV; $n = 5$; $P = 0.006$, repeated measures ANOVA ($\beta = 0.97$); post-hoc Holm-Sidak comparisons). The error bars represent s.e.m. **c**, Example of typical single-cell membrane potential fluctuations during anaesthesia before (top, grey) and after (bottom, black) RWS. Spontaneous action potentials (APs) are rare and visible only during up states. **d**, Example of spontaneous APs before (grey) and after (black) RWS. APs were time-aligned to their respective threshold. **e**, Effect of RWS on AP thresholds, in cells that displayed some spontaneous APs before and after RWS (but not during RWS). AP threshold was computed as the minimal membrane potential value at the time corresponding to the peak of the third derivative of the membrane potential. The Δthreshold was calculated as the difference between the mean AP threshold after RWS and the mean AP threshold before RWS (each circle represents a cell). The level of LTP is independent of Δthreshold ($R^2 = 0.07$, $P > 0.05$, all cells pooled). **f**, The mean threshold for spontaneous AP is not affected by RWS (Pre, -43.7 ± 0.9 mV; Post, -44.6 ± 1.2 mV; $n = 12$; $P = 0.2$, paired t-test ($\beta = 0.13$)). **g**, RWS does not affect the resting membrane potential measured at $I = 0$ during down states (Pre, -71.5 ± 0.4 mV; Post, -71.4 ± 0.6 mV; $n = 12$; $P = 0.8$, paired t-test ($\beta = 0.05$)). **h**, The difference between input resistance (ΔRin) before and after RWS. ΔRin is independent of the level of LTP ($R^2 = 10^{-3}$, $P > 0.05$; each circle represents a cell). Inset, Rin before (grey) and after (dark blue) RWS are estimated by measuring the steady-state resistance of a hyperpolarizing current pulse. **i**, The mean Rin is not affected by RWS (Pre, 46.6 ± 7 MΩ; Post, 50 ± 8 MΩ; $n = 11$; $P = 0.13$, paired t-test ($\beta = 0.22$)). **j**, The number of evoked APs as a function of injected somatic current injection is not significantly modified by RWS (two-way ANOVA, $P > 0.5$, $n = 4$). **k**, The relationship between ΔRin and the relative change in amplitude of PSP_{short}. Each circle represents a cell that was hyperpolarized only during RWS (RWS + Hyper, $R^2 = 0.6$). **l**, The mean Rin is not affected by RWS + Hyper (Pre, 37.4 ± 4 MΩ; Post, 37.7 ± 5 MΩ; $n = 9$; $P = 0.9$, paired t-test ($\beta = 0.05$)). **m**, **n**, The PSP_{short} amplitude evoked by low frequency (0.1 Hz) single whisker deflections, before (Pre), during (Hyper) and after (Post) hyperpolarization (−100 mV). Hyperpolarization increases the PSP amplitude (**m**) due to an enhanced driving force (Pre, 11.3 ± 2.5 mV (average −3 to −1 min); Hyper, 14.7 ± 3 mV; Post (average +1 to +2 min), 11.3 ± 2.4 mV; $n = 4$; $P = 0.002$, one-way repeated-measures ANOVA ($\beta = 0.98$); $^{***}P < 0.001$, Holm-Sidak post-hoc comparisons Hyper versus Pre and Post conditions. However, the integrated PSP is significantly reduced due to the absence of plateau potentials (**n**) (Pre, 0.625 ± 0.2 V·ms; Hyper, 0.335 ± 0.1 V·ms; Post, 0.626 ± 0.2 V·ms; $n = 4$; $P = 0.011$, one-way repeated-measures ANOVA ($\beta = 0.86$); $^{**}P = 0.007$, Holm-Sidak post-hoc comparisons Hyper versus Pre and Post conditions).

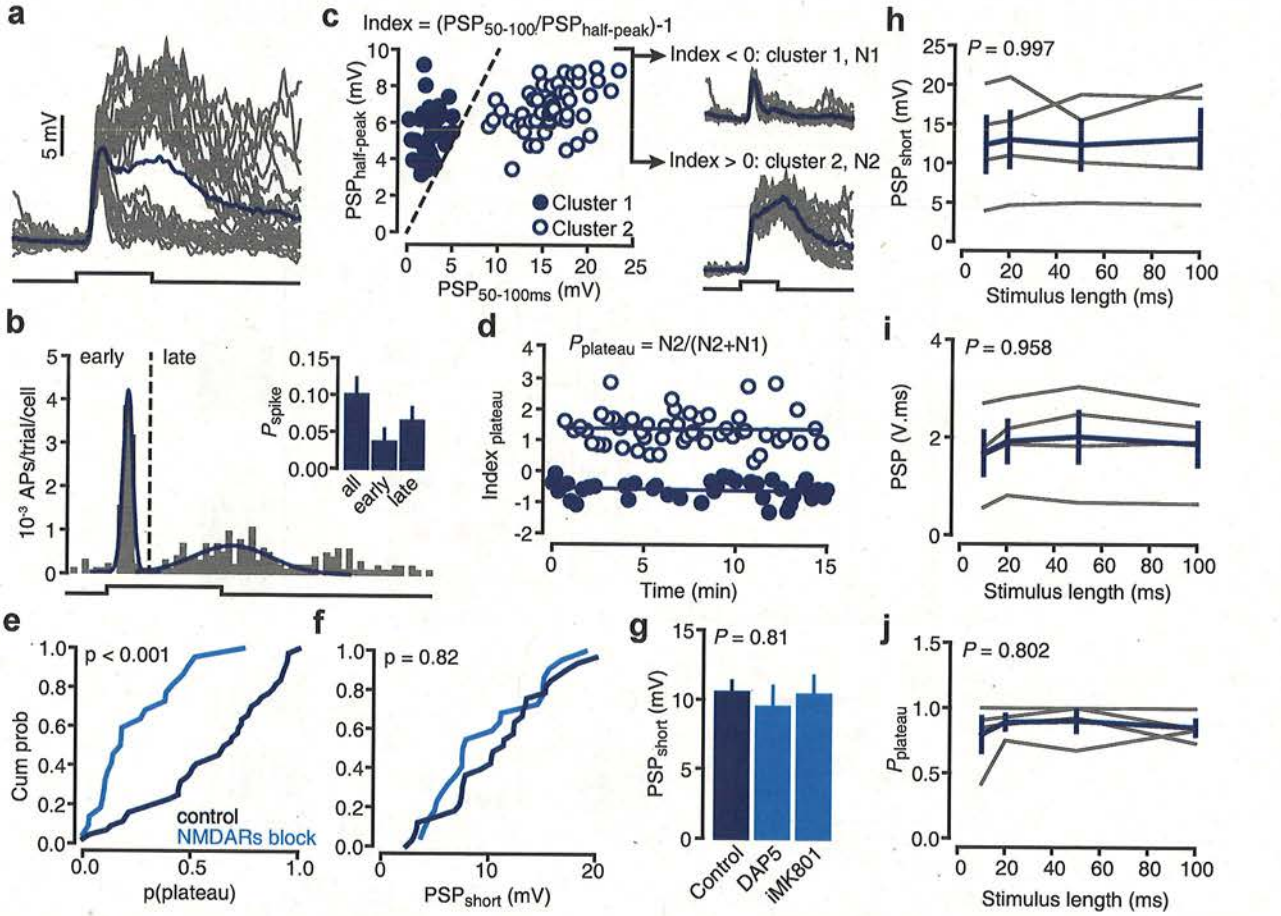

Extended Data Figure 4 | The extraction of whisker-evoked plateau potentials. **a**, Individual PSPs (grey lines) and the average PSP (dark blue line) in a single cell in response to single principal whisker deflections (100-ms deflections). Individual traces show short and long-latency components. The responses to the 30 successive deflections reveal two whisker-evoked PSP populations: one that only contains short-latency PSPs and a second population that contains both short and long-latency PSPs. **b**, Similar to non-spiking cells, the distribution of whisker-evoked actions potentials (APs) also reveals two populations of spikes, based on their onset delay. Inset, for each spiking cell, whisker-evoked spikes were sorted as early and late spikes, according the delay of the first peak of the subthreshold response. The corresponding probabilities were then computed (early, $P = 0.04 \pm 0.02$, $n = 15$; late, $P = 0.06 \pm 0.02$, $n = 15$; $P = 0.345$, z-test). The equal probabilities indicate that L2/3 cells spike as often upon a long-latency depolarization as in response to a short-latency PSP. **c**, Left, for each trial, the relationship between the PSP half-peak amplitude and the average membrane potential between 50 and 100 ms after the onset reveals two distinct clusters. Dotted line represents the identity line. Right, cluster 1 (top) is defined by an index < 0 and consists of PSPs containing only a short latency PSP that quickly returns to the resting membrane potential. Cluster 2 (bottom) is defined by an index > 0 and consists of compound PSPs with short and long-latency components. The long-latency component of the PSP has a strong plateau-like appearance. Therefore, we defined this index as the $\text{Index}_{\text{plateau}}$. **d**, Example of the distribution of clusters 1 and 2 over time. The $\text{Index}_{\text{plateau}}$ was computed from the example shown in **a**. The probability of eliciting plateau potentials in a neuron is calculated by dividing the number of PSPs in cluster 2 (N2) by the total number of PSPs (N1 + N2). **e**, **f**, Blocking NMDARs (light blue) significantly reduced the probability of eliciting plateau potentials as compared to controls (dark blue) (**e**, ks test, $P < 0.001$), but does not affect the amplitude of the short-latency PSP ($\text{PSP}_{\text{short}}$) (**f**, ks test, $P > 0.05$). **g**, Blocking NMDARs by epidural application of DAP5 or intracellular MK801 does not affect the amplitude of $\text{PSP}_{\text{short}}$ (control, 10.5 ± 0.8 mV, $n = 33$; DAP5, 9.5 ± 1.5 mV, $n = 12$; iMK801, 10.3 ± 1.3 mV, $n = 10$; $P > 0.05$, one-way ANOVA ($\beta = 0.05$)). **h–j**, Changes in the length of the whisker deflection period (stimulus length) do not affect the whisker-evoked mean $\text{PSP}_{\text{short}}$ amplitude (**h**), the mean PSP integral (**i**), or the probability to elicit plateau potentials (**j**) ($n = 4$, $P > 0.05$, one-way ANOVA ($\beta = 0.05$)). Values in **b** and **g–j** are represented as the mean $\pm$ s.e.m.

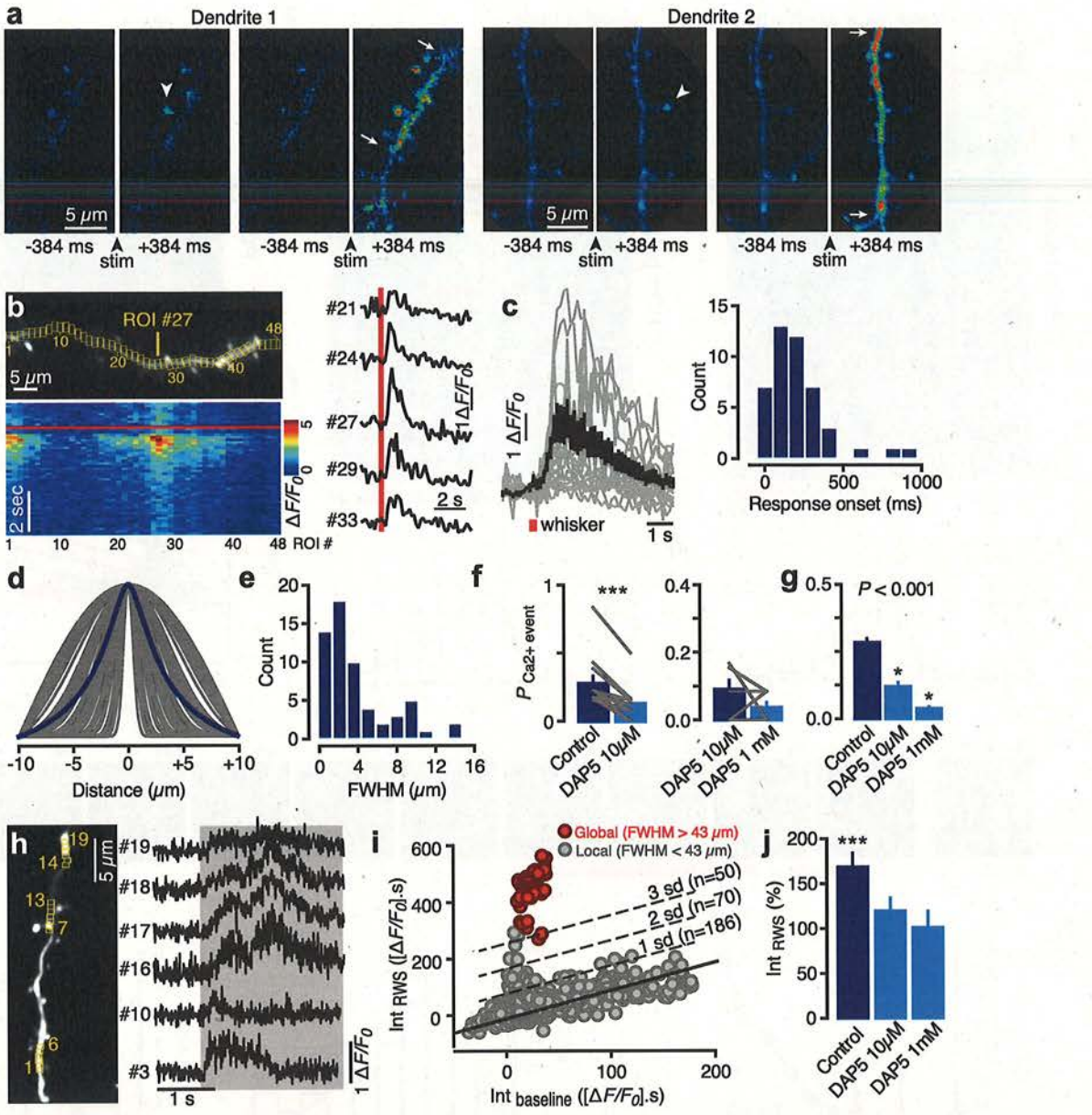

Extended Data Figure 5 | NMDAR-dependent whisker-evoked Ca^{2+} events in L2/3 pyramidal neuron dendritic tufts. **a**, Examples of single whisker deflection-evoked Ca^{2+} responses in dendritic spines (arrowheads) and dendritic shafts (regions in between arrows). **b**, Top left, GCaMP6 s fluorescence standard deviation image with ROIs. Bottom left, raster plot of $\Delta F/F_0$ for each ROI in the top panel (aligned). Red bar represents the whisker stimulation onset. Right, $\Delta F/F_0$ traces of some ROIs from **a**. **c**, Left, time course of mean dendritic Ca^{2+} response in individual dendritic branches upon a single whisker deflection (2–5 trials per branch, $n = 48$ dendritic branches, $n = 9$ mice). Grey, individual branches. Black, average response. Right, distribution of response onset times. **d**, Averaged (blue thick line) and individual (grey lines) Gaussian fits of local responsive regions in dendritic shafts. **e**, Distribution of the FWHM of the Guassian fits in **d**. **f**, Epidural application of DAP5 (10 μM) significantly reduces whisker-evoked local dendritic Ca^{2+} response probabilities. The subsequent addition of 1 mM DAP5 in some cases further reduced probabilities and in others did not show an additive effect (control, 0.29 ± 0.06, DAP5 (10 μM), 0.14 ± 0.04; $n = 16$ branches, $n = 3$ mice; $P = 0.002$, Wilcoxon signed-rank test; DAP5 (10 μM), 0.08 ± 0.03; DAP5 (1 mM), 0.04 ± 0.02; $n = 9$ branches, $N = 2$ mice; $P = 0.37$, Wilcoxon signed-rank test). **g**, On average, DAP5 significantly reduces whisker-evoked local dendritic Ca^{2+} response probabilities (control, 0.28 ± 0.03; DAP5 (10 μM), 0.12 ± 0.03; DAP5 (1 mM), 0.04 ± 0.02; Kruskal–Wallis one-way ANOVA on ranks; post-hoc Dunn's comparisons versus control condition, $P < 0.05$)). **h**, Left, GCaMP6 s fluorescence standard deviation image with ROIs. Right, $\Delta F/F_0$ traces of some ROIs from the left panel. Grey box represents the RWS period. **i**, Integrated $\Delta F/F_0$ in dendritic branches during RWS (0–15 s) as a function of the response before RWS (0–15 s baseline). Each circle represents a single dendritic branch. Red, global events (responses spanning the whole field of view, minimally 43 μm); grey, local events (responses spanning a portion of the field of view, maximally 43 μm). Black line indicates the identity line. RWS significantly increases $\Delta F/F_0$ for a substantial number of branches. **j**, The average integrated $\Delta F/F_0$ in dendritic branches during RWS (0–15 s) is significantly reduced upon topical application of DAP5 (control, 168 ± 15%; DAP5 (10 μM), 119.6 ± 14.5%; DAP5 (1mM), 100.1 ± 18.5%; paired t-test).

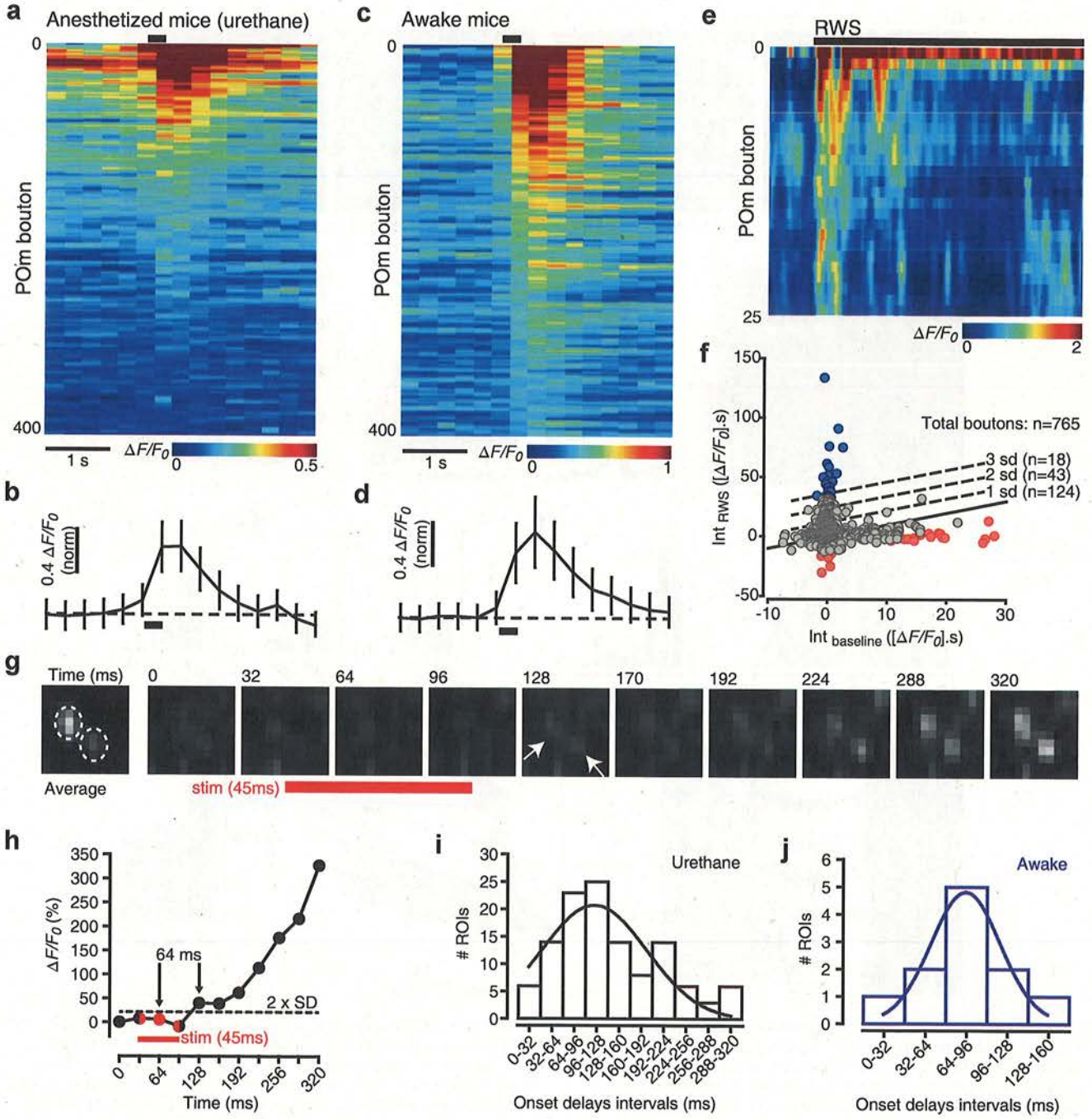

Extended Data Figure 6 | Whisker-evoked activity in cortical POm efferents in anaesthetized and awake mice. **a**, **c**, Raster plots of average Ca^{2+} responses ($\Delta F/F_0$) in 400 different cortical POm efferent boutons over 10–20 successive (0.1 Hz) bursts of 5 whisker deflections (20 Hz, black bar) in anesthetized mice (**a**) and in awake mice (**c**). **b**, **d**, Average whisker-evoked responses over 400 boutons under anaesthesia (**b**) and under wakefulness (**d**). **e**, Raster plot for 25 of the most active boutons (out of 765) upon RWS. Black bars indicate the period of RWS (1 min). The Ca^{2+} response in some boutons remains elevated over the whole RWS period. **f**, Integrated Ca^{2+} responses of individual boutons during RWS (0–15 s) as a function of their responses before RWS (15 s baseline). Each circle represents a single bouton. The 25 most and least responsive boutons are in blue and red respectively. Black line indicates the mean relationship (linear fit). Dotted lines indicate the relationship at various standard deviations from the fit. A substantial proportion of boutons (16%; 124 out of 765) display RWS/baseline ratios larger than 1 s.d. from the mean. **g**, Time-lapse image of fluorescence change representing Ca^{2+} responses in axonal boutons (dotted circles) upon a single whisker deflection (red bar; 45 ms). Response onsets are indicated by arrows. Scale bar represents 1 μm. **h**, Example of the response curve of the boutons in **g**. Response onset latency was defined as the time frame in which $\Delta F/F_0$ exceeded 2 × s.d. of the baseline. **i**, **j**, Distributions of response onset latencies under anaesthesia (black, 120 trials, $n = 5$ boutons, $n = 3$ mice) and under wakefulness (blue, 11 trials, $n = 5$ boutons, $n = 3$ mice).

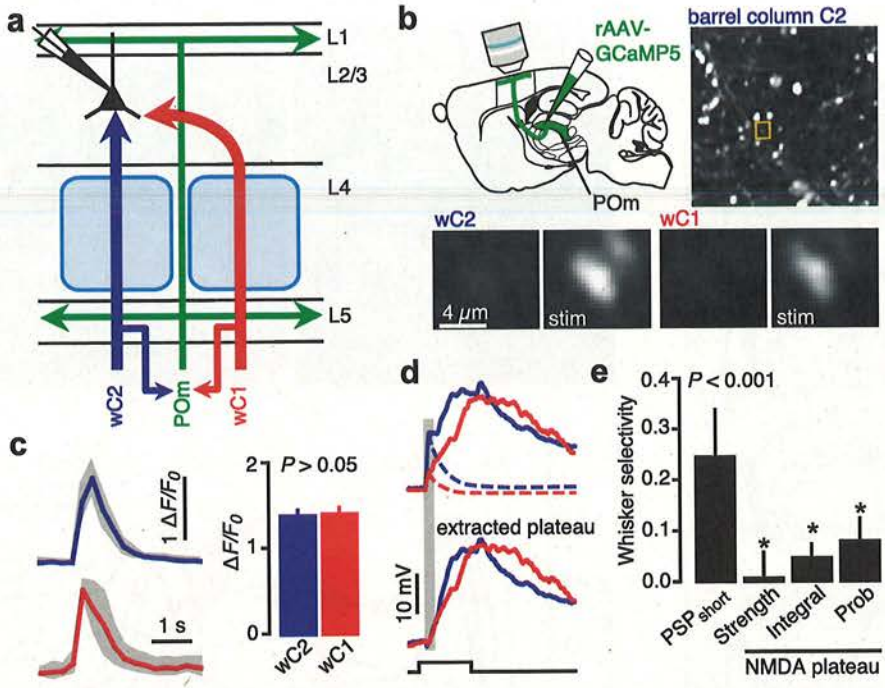

Extended Data Figure 7 | Plateau potentials in L2/3 pyramidal neurons and POm-efferent activity are not whisker-specific. **a**, Schematic of the experiment. Whole-cell recordings are targeted to the C2 barrel column. Responses are recorded upon deflection of the C2 whisker (wC2, principal whisker, PW, blue) or the C1 whisker (wC1, surrounding whisker, SW, red). **b**, Right, example of 2PLSM images of POm boutons expressing GCaMP5. Both the PW (wC2) and SW (wC1) evoke a Ca^{2+} response. **c**, Left, the average Ca^{2+} transient ($\Delta F/F_0$) for both whisker deflections (shadows represent the s.d.). Right, mean $\Delta F/F_0$ upon deflection of the PW (wC2) and SW (wC1) (wC2, 1.37 ± 0.07, $n = 5$; wC2, 1.38 ± 0.08, $n = 5$; $P > 0.05$). This confirms that POm activity is not selective for whiskers. Values are represented as mean ± s.e.m. **d**, Top, example of the average PSP evoked by the PW (blue) or the SW (red). To estimate the integral of the plateau potential (bottom), the decay of the first component is fitted with a single exponential and subtracted from the average of PSPs containing both short and late-latency components (cluster 2 in Extended Data Fig. 4c). **e**, For each parameter, whisker selectivity is defined by the ratio between the PW and SW: (PW − SW)/(PW + SW). All parameters related to plateau potentials (plateau strength, plateau integral, probability) are not specific to either one of the whiskers. In contrast, and as expected, the short-latency PSP amplitude (PSP_{short}) is higher (and thus more selective) for the PW (PSP_{short}, 0.25 ± 0.09, $n = 27$; plateau strength, 0.006 ± 0.05, $n = 26$; plateau integral, 0.04 ± 0.02, $n = 26$; plateau probability, 0.07 ± 0.04; $n = 27$; $P < 0.001$, one-way ANOVA on ranks; $^*P < 0.05$, post-hoc Dunn's comparisons versus PSPshort condition). As the amplitude of short-latency PSPs is whisker-selective and plateau potentials are not, it is conceivable that POm associated synaptic pathways are responsible for mediating whisker-evoked plateau potentials.

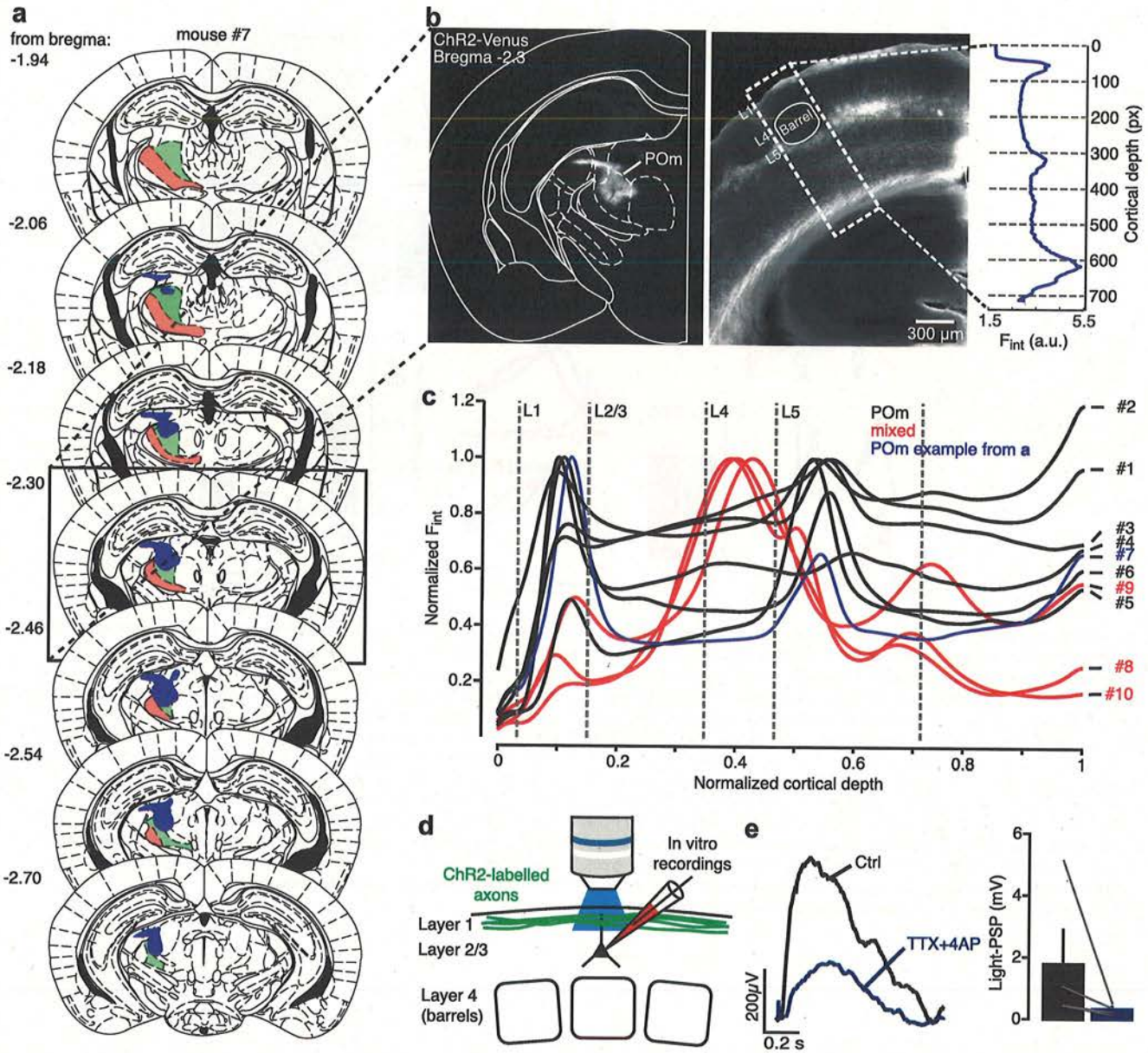

Extended Data Figure 8 | AAV-mediated expression of ChR2-Venus in the POm nuclei of the thalamus and their efferents in L1. **a**, Representative example of the ChR2-Venus expression profile in the mouse thalamus. The expression profile of ChR2-Venus is depicted in blue, POm nuclei in light green, and the VPm in light red. **b**, Left, example of a cortical slice with ChR2-Venus fluorescence in the caudal sector of the POm (bregma −2.3). Right, an image of the fluorescence profile in the somatosensory cortex in the same animal as on the left. Fluorescence intensities (F_{int}) were measured as a function of cortical depth (in pixels (px)) by summing all pixels within the dotted rectangle over the short axis (pixel size = 1.85 µm). The fluorescence intensity profile is similar to the cortical projection pattern of efferents from the caudal sector of the POm (Supplementary Note 4). **c**, Plot comparing the intensity profiles of 10 different animals in which injections were aimed at the POm nuclei in the thalamus. Animals classified as bearing expression profiles in the barrel cortex that are typical of POm projections (Supplementary Notes 4 and 5) displayed distinct fluorescence peaks in L1 (0.04 – 0.12 normalized depth) and L5 (0.48 – 0.7 normalized depth; $n = 7$, black lines and blue line). In contrast, animals with a (additional) distinct peak in L4 (0.36 – 0.48 normalized depth; $n = 3$, red lines) were considered as having at least some spurious expression in VPm, and were thus excluded from the analysis in Fig. 3. The classification matched the expression profiles in the thalamus (Supplementary Information). **d**, **e**, Assessment of POm mediated synaptic inputs onto L2/3 neurons in acute cortical slice preparations. **e**, Schematic of the slice experiment. L2/3 pyramidal neurons were recorded during local photostimulation (through the objective) of ChR2-expressing POm axons. **f**, Left, example of photostimulation-evoked PSPs in a single L2/3 cell under control conditions and following bath application of TTX and 4AP. Right, average PSP amplitudes in controls and after TTX + 4AP application (control, 1.8 ± 1.1; TTX + 4AP, 0.31 ± 0.08, $n = 4$, $P = 0.125$, paired Wilcoxon signed-rank test).

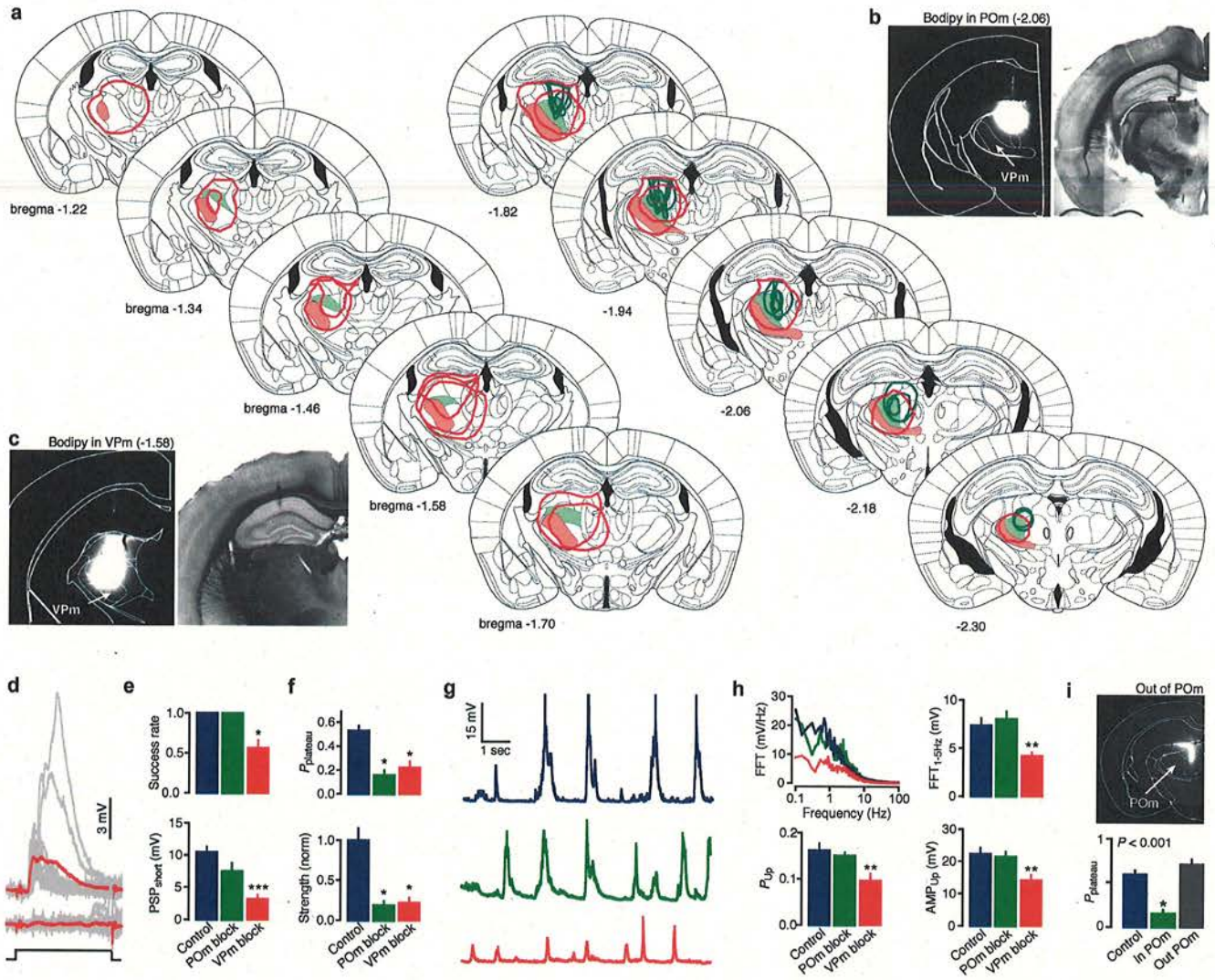

Extended Data Figure 9 | The spread of fluorescent muscimol in thalamic nuclei. **a**, Coronal diagrams of the mouse brain adapted from the Paxinos atlas[41] including the POm (light green) and VPm (light red) nuclei at various posterior distances from bregma. Each red or green line represents the maximal spread of fluorescent muscimol, as assessed using whole field epifluorescence microscopy (Olympus; ×20 and ×60 objective) and Neurolucida (Microbrightfield) reconstructions. Green lines (8 mice) represent injections that were confined to the POm. Red lines (3 mice) represent injections that infiltrated both POm and VPm thalamic nuclei. **b, c**, Examples of a muscimol injection in the caudal part of the POm (**b**) and an injection that spread into both POm and VPm nuclei (**c**). **d**, Examples of whisker-evoked PSPs in L2/3 neurons of mice in which muscimol was present in both POm and VPm. Successes (top) and failures (bottom) are shown. Grey lines, individual trials, light red lines, average. **e**, Blocking activity in VPm decreases the whisker-evoked PSP success rate (top; control, 1 ± 0, $n = 33$; POm block, 1 ± 0, $n = 9$; POm + VPm block, 0.56 ± 0.1, $n = 7$; $P < 0.001$, one-way ANOVA on ranks; $^*P < 0.05$, post-hoc Dunn's comparisons versus control condition), as well as PSP_{short} amplitudes (bottom; control, 10.5 ± 0.8, $n = 33$; POm block, 7.5 ± 1.3, $n = 9$; POm + VPm block, 3.15 ± 0.6, $n = 7$; $P < 0.001$, one-way ANOVA; $^*P < 0.05$, post-hoc Holm-Sidak's comparisons versus control condition). **f**, Blocking POm + VPm or POm only significantly decreases the probability of plateau potentials (top; control, 0.35 ± 0.04, $n = 33$; POm block, 0.16 ± 0.04, $n = 9$; VPm block: 0.22 ± 0.05, $n = 7$; $P < 0.001$, one-way ANOVA on ranks; $^*P < 0.05$, post-hoc Dunn's comparisons versus control condition), and the normalized plateau strength (bottom; control, 1 ± 0.15, $n = 33$; POm block, 0.19 ± 0.05, $n = 9$; POm + VPm block, 0.22 ± 0.07, $n = 7$; $P < 0.001$, one-way ANOVA on ranks; $^*P < 0.05$, post-hoc Dunn's comparisons versus control condition). **g**, examples of single-cell spontaneous membrane potential fluctuations during anaesthesia in controls (top) and upon muscimol injections in POm (middle) or POm + VPm (bottom). **h**, Top left, FFT of membrane potentials in controls (dark blue) and after muscimol injection in POm (green) or POm + VPm (light red). Top right, Blocking POm + VPm significantly decreases the 1–5-Hz range in the FFT (control, 7.33 ± 0.76, $n = 14$; POm block, 8.03 ± 0.81, $n = 8$; VPm block, 4.2 ± 0.37, $n = 7$; $P = 0.008$, one-way ANOVA; $^*P < 0.05$, post-hoc Holm-Sidak's comparisons versus control condition). Bottom, blocking POm + VPm significantly decreases the probability of spontaneous up states (left (P_{up}); control, 0.16 ± 0.016, $n = 14$; POm block, 0.15 ± 0.008, $n = 8$; POm + VPm block, 0.09 ± 0.016, $n = 7$; $P = 0.023$, one-way ANOVA; $^*P < 0.05$, post-hoc Holm-Sidak's comparisons versus control condition), as well as the amplitude of spontaneous up states (right (AMP_{up}); control, 22.3 ± 1.9, $n = 14$; POm block, 21.5 ± 1.6, $n = 8$; POm + VPm block, 14.1 ± 1.7, $n = 7$; $P = 0.02$, one-way ANOVA; $^*P < 0.05$, post-hoc Holm-Sidak's comparisons versus control condition). **i**, Animals in which muscimol injections in the medial posterior thalamus did not infiltrate the POm (out of POm) were used as a negative controls ($n = 6$). In these animals, the probability of eliciting plateau potentials ($P_{plateau}$) remained equal to controls. The probability was significantly reduced, only when muscimol was correctly targeted to POm (control, 0.6 ± 0.04, $n = 44$; +muscimol In POm, 0.16 ± 0.04, $n = 9$; +muscimol Out POm, 0.72 ± 0.06, $n = 8$; $P < 0.001$, one-way ANOVA on ranks; $^*P < 0.05$, post-hoc Dunn's comparisons versus control condition). The values represent the mean ± s.e.m.